

Contrasted turbulence intensities in the Indonesian Throughflow: a challenge for parameterizing energy dissipation rate

Bouruet-Aubertot Pascale ^{1,*}, Cuypers Yannis ¹, Ferron Bruno ⁴, Dausse Denis ¹, Ménage Olivier ²,
Atmadipoera Agus ³, Jaya Indra ³

¹ Sorbonne Université- UPMC Université Paris 06- LOCEAN, Paris, France

² LOPS-Ifremer, Plouzané, France

³ IPB, Bogor, Indonesia

* Corresponding author : Pascale Bouruet-Aubertot, email address : pba@locean-ipsl.upmc.fr

Abstract :

Microstructure measurements were performed along two sections through the Halmahera Sea and the Ombai Strait and at a station in the deep Banda Sea. Contrasting dissipation rates (ϵ) and vertical eddy diffusivities (K_z) were obtained with depth-averaged ranges of $\sim[9 \times 10^{-10} - 10^{-5}] \text{ W kg}^{-1}$ and of $\sim[1 \times 10^{-5} - 2 \times 10^{-3}] \text{ m}^2 \text{ s}^{-1}$, respectively. Similarly, turbulence intensity, $I = \epsilon / (vN^2)$ with v the kinematic viscosity and N the buoyancy frequency, was found to vary seven orders of magnitude with values up to 107. These large ranges of variations were correlated with the internal tide energy level, which highlights the contrast between regions close and far from internal tide generations. Finescale parameterizations of ϵ induced by the breaking of weakly nonlinear internal waves were only relevant in regions located far from any generation area ("far field"), at the deep Banda Sea station. Closer to generation areas, at the "intermediate field" station of the Halmahera Sea, a modified formulation of MacKinnon and Gregg (2005) was validated for moderately turbulent regimes with $100 < I < 1000$. Near generation areas marked by strong turbulent regimes such as "near field" stations within strait and passages, ϵ is most adequately inferred from horizontal velocities provided that part of the inertial subrange is resolved, according to Kolmogorov scaling.

Keywords : Turbulence, Internal tides, Vertical mixing, Parameterization, Indonesian seas, Microstructure measurements

27 1 INTRODUCTION

28 The Indonesian seas are a key region of the ocean as they provide a passage at low lat-
29 itude for Pacific waters toward the Indian ocean (e.g., [Sprintall et al., 2004](#), see Figure
30 1 of this paper). This inflow, called the Indonesian Throughflow, significantly impacts
31 the thermohaline circulation (e.g., [Gordon and Fine, 1996](#)). Indeed, it contributes to the
32 poleward heat flux as Pacific waters are injected into the Indian Ocean and exit within
33 the poleward flowing Aghulas current ([Gordon, 2005](#)). In the pycnocline, Pacific waters
34 flowing through the Indonesian seas get progressively cooler and fresher (e.g., [Gordon,](#)
35 [2005](#); [Atmadipoera et al., 2009](#)). These water mass transformations result from an in-
36 tense vertical mixing. They have a significant impact not only through the water column
37 but also on the atmosphere as the cooling of surface waters can affect the onset of deep
38 atmospheric convection (e.g., [Gordon, 1986](#); [Koch-Larrouy et al., 2008](#)).

39

40 The strong turbulent mixing in the Indonesian Seas was evidenced indirectly by [Ffield](#)
41 [and Gordon \(1996\)](#) from the sea surface cooling it induces. Moreover, the temperature
42 signature was found to vary at fortnightly and monthly tidal periods, thus suggesting
43 that vertical mixing is mostly driven by the strong tides present in the area. Other
44 estimates that used the variance of temperature at finescale ($\sim 2\text{-}10\text{ m}$) as a proxy of
45 mixing ([Ffield and Robertson, 2005, 2008](#); [Robertson, 2010](#)) showed that the finescale
46 variance is larger in straits and on shelf-slope boundaries where internal tide generation
47 is strong. However, apart from these indirect inferences on the distribution of mixing

48 and its possible relationship with internal tides, there has been no direct measurements
49 of the dissipation rate of turbulent kinetic energy at microscale focusing on the role of
50 tides. Microstructure measurements were only performed in the Banda Sea (Alford
51 et al., 1999; Alford and Gregg, 2001). In this region far from any generation area of
52 internal tides, mixing induced by a baroclinic near-inertial wave was evidenced with
53 mean values in the thermocline of the order of $10^{-5} \text{ m}^2 \text{ s}^{-1}$ for K_z and $10^{-8} \text{ W kg}^{-1}$ for ϵ
54 (Alford et al., 1999; Alford and Gregg, 2001).

55

56 Previous observations aimed at characterizing volume and heat transports across the
57 numerous straits of the Indonesian seas (JADE, WOCE and INSTANT; e.g., Sprintall
58 et al., 2004; Schiller et al., 2010; Gordon et al., 2010). The main information on tides
59 relies on numerical models (e.g., Robertson and Field, 2008; Robertson, 2010; Nagai and
60 Hibiya, 2015) and satellite altimetry for the barotropic tide (e.g., Egbert and Ray, 2000,
61 2003). Conversion rates from barotropic to baroclinic tides show that the Indonesian
62 seas are one of the main regions for internal tide generation (Lyard and Le Provost, 2002)
63 with a power value of 0.11 TW that represents about 10% of the global power value (see
64 as well Simmons et al., 2004). The strength of internal tides varies spatially depending
65 on generation sites and interference patterns (e.g., Robertson, 2010; Rainville et al., 2010).
66 As opposed to deep and large interior seas such as the Banda Sea, internal tides are
67 enhanced within the small and shallow semi-enclosed seas as a result of numerous inter-
68 actions between internal tidal beams originating from sills and shelf-slopes, wave-wave
69 interactions and scattering (Robertson and Field, 2008; Buijsman et al., 2012; Mathur
70 et al., 2014; Gayen and Sarkar, 2011). These differences in internal tide strength suggest

71 that different mechanisms of energy transfers toward small scales are at play : weakly
72 non linear wave-wave interactions of characteristic time scale much larger than the buoy-
73 ancy period or more non-linear processes of smaller characteristic time scales.

74

75 The main objectives of the INDOMIX cruise were to estimate tidal mixing and provide
76 a finescale parameterization of ϵ in this area. Koch-Larrouy et al. (2015) showed that tidal
77 mixing is intensified in regions of rough topography and that subsurface mixing leads to
78 significant surface cooling. They compared tidal mixing estimates from microstructure
79 measurements and indirect estimates from geochemical tracers and finescale estimates
80 from Thorpe scales all along the cruise path based on expandable bathythermograph,
81 XBT, and conductivity-temperature-depth, CTD, measurements. None of the above
82 mentioned studies focused on the relevance of finescale parameterizations of ϵ with di-
83 rect observations of ϵ . The use of repeated stations over two M_2 cycles at locations with
84 contrasting internal tide energy levels makes this study a unique opportunity to closely
85 examine the relevance of finescale parameterizations of ϵ using micro- and fine-structure
86 observations of currents, temperature and salinity. These finescale parameterizations
87 of ϵ induced by internal wave breaking rely on two key assumptions: firstly, that the
88 turbulent kinetic energy results from an energy cascade toward small-scales driven by
89 nonlinear wave-wave interactions, and secondly, that there is a balance between turbu-
90 lent kinetic energy production, dissipation rate and buoyancy flux (e.g., Polzin et al.,
91 2014). Hence, they do not apply to other situations that may lead to wave breaking such
92 as boundary layer physics and hydraulic jumps or internal wave breaking resulting from
93 a linear propagation in spatially inhomogeneous environments as underlined by Polzin

94 [et al. \(2014\)](#). Moreover, applying the parameterization when turbulence is produced by
95 strong nonlinear interactions may, in some cases, lead to underestimates of ϵ , which can
96 be crucial for large scale circulation issues ([Polzin et al., 2014](#)). The contrasting internal
97 tide energy levels and the wide range of turbulence intensities of the INDOMIX measure-
98 ments offer the opportunity to evaluate two main types of finescale parameterizations
99 designed for different dynamical conditions. The first type is based on the assumption
100 that energy is transferred toward small dissipative scales through a cascade initiated by
101 weakly non-linear interactions between internal waves (e.g., [McComas and Müller, 1981](#);
102 [Henyey et al., 1986](#)). These formulations have been improved during the last decades
103 as detailed in a recent review by [Polzin et al. \(2014\)](#). Alternatively, the second type of
104 parameterization is designed for situations where one frequency constituent or low ver-
105 tical mode dominates ([MacKinnon and Gregg, 2003](#)). This parameterization was first
106 validated in a coastal area ([MacKinnon and Gregg, 2003](#)) and then in an open-ocean area
107 in presence of strong internal tide ([Xie et al., 2013](#)). Our purpose is to evaluate the rel-
108 evance of these finescale parameterizations in different energetic regimes and levels of
109 turbulence as observed in the ITF using our set of dissipation rates based on microstruc-
110 ture data.

111

112 The outline is the following: we present the dataset and methods in section 2 followed
113 by an overview of internal tides which introduces the different dynamical context of
114 the stations, dissipation rate and vertical eddy diffusivity in section 3. In section 4, we
115 test existing finescale parameterizations. We also show that, for strongly turbulent re-
116 gions, the dissipation rate can be directly inferred from the observed horizontal velocity

117 differences along the vertical direction. Finally, results are summarized and discussed in
118 section 5.

119

120 2 DATA AND METHODS

121 The INDOMIX cruise took place from 11th to 19th July 2010 during spring tides. The
122 first three stations were occupied in the Halmahera Sea (Figure 1), a region of strong
123 barotropic to baroclinic tidal conversion (e.g., Nagai et al., 2017). The first and third
124 stations, S_1 and S_3 , were located near straits where a strong internal tide generation is
125 expected. The second station, S_2 , was in a deeper region located ~ 40 km away from
126 any generation area. These three stations emphasized the contrast between near-field
127 and intermediate-field areas. Station S_4 , located far from any boundary and generation
128 areas in a deep region of the Banda Sea, is the only far-field station. Station S_5 located
129 in one of the most energetic area regarding internal tides, the Ombai Strait, is another
130 near-field station (Figure 2).

131 2.1 CTD and LADCP

132 CTD measurements were obtained using a Seabird SBE911 instrument. Data were aver-
133 aged over 1-m bins to filter out spurious salinity peaks. The salinity standard deviation

134 between the CTD and the bottle samples was 0.01. The CTD temperature standard de-
135 viation was 0.002 °C according to Seabird factory calibration (Atmadipoera et al., 2017).
136 Simultaneously, currents were measured from a broadband 300 kHz RDI lowered acous-
137 tic Doppler current profiler (LADCP). LADCP data were processed using the Visbeck
138 velocity inversion method (Visbeck, 2002) and provided vertical profiles of horizontal
139 currents at 8 m resolution. At each station, except that in the Banda Sea (station S₄),
140 CTD/LADCP profiles were repeated over two semi-diurnal tidal cycles with a maxi-
141 mum time interval of 3 hours with microstructure profiles in between (see Figure 1). In
142 addition, the ship was equipped with two ADCPs with frequencies 150kHz and 75kHz.
143 Data from the 75kHz ship-ADCP (SADCP) used in this study provided currents at a
144 15 m vertical resolution after processing.

145 2.2 Dissipation rate from microstructure measurements and diffusivity estimates

146 For each station, microstructure measurements were collected using a vertical microstruc-
147 ture profiler, VMP6000 (see Table 1). The dissipation rate of turbulent kinetic energy (ϵ)
148 was inferred from centimeter-scale shear measurements. Note that, depending on the
149 VMP weights used for its descent, the averaged VMP fall rate varied from one station
150 to the other, typically from 0.5 m s⁻¹ within passages to 1 m s⁻¹ at the Banda Sea station.
151 Variations in the VMP fall rate within each profile were small, typically of the order of
152 1%, except at the very end of the profile which was not considered in the analysis. ϵ was
153 inferred from the variance of the shear within the inertial range, typically within meter

154 to centimeter scales. The experimental spectrum was next compared to the empirical
 155 spectrum, the Nasmyth spectrum (Nasmyth, 1970), which enabled validation of the esti-
 156 mate of ϵ (e.g., Ferron et al., 2014). The noise level was below $10^{-11} \text{ W kg}^{-1}$. ϵ was first
 157 computed over a 1 m depth interval and then smoothed with a 10-m moving average. A
 158 total number of 36 profiles unevenly distributed among stations was carried out (Table
 159 1).

160

161 The diapycnal diffusivity (K_z) is commonly inferred from the kinetic energy dissipa-
 162 tion rate using the Osborn (1980) relationship:

$$K_z = \Gamma \epsilon N^{-2} \quad (1)$$

163 where Γ is a mixing efficiency defined as the ratio between the buoyancy flux and the dis-
 164 sipation rate, $\Gamma = -\frac{g}{\rho_0} \frac{\overline{\rho' w'}}{\epsilon}$ with w' and ρ' the vertical velocity and density fluctuations,
 165 and N is the buoyancy frequency. N was first computed from the sorted density profile,
 166 $N = \sqrt{-\frac{g}{\rho_0} \frac{d\rho_{\text{sorted}}}{dz}}$, with $dz = 1 \text{ m}$, and then smoothed using a 10-m moving average for
 167 consistency with ADCP data. Data from the VMP SBE sensors were used in most cases
 168 except when spurious measurements were obtained in which cases data from the rosette
 169 interpolated at the time of VMP profiles were taken as a substitute. N^2 values below
 170 a threshold value of 10^{-7} s^{-2} were excluded for the computation of K_z , I and finescale
 171 parameterization estimates, assuming a precision of $\sim 10^{-4} \text{ kg m}^{-3}$ for density. In mixing
 172 studies, Γ is generally set to 0.2, which corresponds to a critical flux Richardson number
 173 $R_{\text{crit}} = 0.17$ (Osborn, 1980). Shih et al. (2005) and more recently Bouffard and Boeg-

174 man (2013) examined the relevance of the Osborn relation as a function of turbulence
 175 intensity:

$$I = \frac{\epsilon}{\nu N^2} \quad (2)$$

176 where ν is the molecular viscosity. This ratio is a measure of the relative importance
 177 of destabilizing effects (turbulence) and stabilizing effects (stratification and viscosity).
 178 Alternatively, in terms of time scales, it is the squared ratio of the buoyancy time scale
 179 ($1/N$) and the Kolmogorov time scale, namely the dissipation time scale of eddies at the
 180 Kolmogorov scale ($\sqrt{\nu/\epsilon}$). Shih et al. (2005) gave evidence of three regimes according to
 181 the I values: the energetic regime that corresponds to $I > 100$, the intermediate regime
 182 for $7 < I < 100$, and the diffusive regime for $I \leq 7$ in which case the diffusivity reduces
 183 to the molecular value. Shih et al. (2005) showed in a numerical study that the Osborn
 184 relationship overestimated K_z for the energetic regime ($I \geq 100$) and proposed a new
 185 parameterization of K_z for this regime. A few years later, Bouffard and Boegman (2013)
 186 proposed a refined parameterization of K_z based on in-situ microstructure measurements
 187 in lakes. They kept the three main regimes defined by Shih et al. (2005) but introduced
 188 two sub-regimes in the diffusive regime, a molecular regime for the smallest I values,
 189 $I < 1.7$, and a buoyancy-controlled regime, $1.7 \leq I \leq 8.5$. The formulations of K_z for
 190 these regimes are given by:

- 191 • $K_z = 10^{-7} \text{ m}^2 \text{ s}^{-1}$ within the diffusive sub-regime, $I < 1.7$
- 192 • $K_z = \frac{0.1}{7^{1/4}} \nu I^{3/2}$ within the buoyancy controlled sub-regime, $1.7 \leq I \leq 8.5$
- 193 • $K_z = 0.2\nu I$, i.e. the Osborn relationship within the intermediate regime, $8.5 \leq I \leq$

- 195 • $K_z = 4\nu I^{1/2}$ within the energetic regime, $I > 400$

196 This parameterization is subject to controversy in the field measurement community
 197 (e.g., [Gregg et al., 2012](#)) who argued that the reduced mixing efficiency obtained in
 198 laboratory experiments and numerical simulations was an artefact. Their first concern
 199 dealt with the way turbulence was driven and the second to the fact that part of the
 200 downward transport from the outer scale was not resolved in the simulations since the
 201 size of the domain was of the same order as the Ozmidov scale which defines the upper
 202 bound of the inertial range. [Bouffard and Boegman \(2013\)](#) addressed these questions
 203 and showed that the [Shih et al. \(2005\)](#) parameterization held within a factor of 2 based
 204 on observations collected in lakes. The decrease in mixing efficiency with increasing
 205 turbulence intensity was also evidenced in the ocean (e.g., [Bluteau et al., 2013](#)). Hence,
 206 we applied the Bouffard and Boegman parameterization in this study while the Osborn
 207 estimate was computed for comparison.

208 2.3 Internal tide generation and propagation

209 *Linear approximation of the generating force for internal tide*

The internal tide generation was inferred from the generating force at the bottom following the linear approximation (e.g., [Baines, 1982](#)) that reads:

$$\|\vec{F}\| = \frac{N^2}{\omega} \frac{\|\vec{Q} \cdot \nabla h\|}{h}$$

210 where $N^2 = 2.9 \times 10^{-6} \text{ rad}^2 \text{ s}^{-2}$, ω is the tidal frequency, and $\|\vec{Q}\|$ is the barotropic tidal
 211 flux and h the depth. The barotropic tidal flux was inferred from the $1/30^\circ \times 1/30^\circ$

212 global inverse tidal model TPXO (Egbert and Erofeeva, 2002) for two main constituents,
213 the diurnal K_1 and the semi-diurnal M_2 .

214

215 *Idealized two-dimensional simulations*

216 Further insights on internal tides were inferred from a two-dimensional linear model
217 of internal tide generation and propagation (Gerkema et al., 2004). The model as-
218 sumed spatial uniformity in the direction perpendicular to the 2D vertical section while
219 geostrophic currents were taken into account through the thermal wind balance. The
220 model was applied and validated against in-situ measurements in the Bay of Biscay
221 (Gerkema et al., 2004) as well as in the Mozambique channel where the influence of
222 eddies on internal tide propagation is significant (Manders et al., 2004). The horizontal
223 resolution was 400 m while in the vertical direction a Chebyshev collocation method was
224 used involving 60 polynomial functions. The inputs for the model were the barotropic
225 flux, the topographic profile along the section and the buoyancy field, N . The barotropic
226 flux was prescribed at the boundaries using TPXO outputs for the semi-diurnal M_2
227 and diurnal K_1 constituents. The topographic profile was inferred from the Smith and
228 Sandwell bathymetry and interpolated on the 400 m resolution grid of the model. The
229 buoyancy field was inferred from in-situ data collected during the cruise: the time aver-
230 aged N^2 profile smoothed over a 30 m window was considered. The Gerkema's model
231 was applied to the 2D-section of the Halmahera Sea passing through stations S_1 , S_2 and
232 S_3 . The model was also applied to a section passing through the Ombai strait.

233 2.4 Finescale parameterization

234 In the absence of microstructure measurements, ϵ is classically inferred from a finescale
 235 parameterization which relates properties of the internal wave field to the energy dissi-
 236 pation rate. This relationship depends on the dynamics of the internal wave field that
 237 controls energy transfers toward small scales.

238

239 Typically, when the time scale of non-linear interactions is larger than the period of the
 240 waves, which is the case of an internal wave field close to the GM model, ϵ scales like E^2 ,
 241 where E is the energy level of the internal wavefield. Different formulations have been
 242 proposed either as a function of energy, shear ($S = \sqrt{(\partial_z v_x)^2 + (\partial_z v_y)^2}$ with v_x and v_y
 243 the zonal and meridional velocity components) and/or strain ($\partial_z \zeta$ with ζ the isopycnal
 244 displacement) (e.g., [Gregg et al., 2003](#); [MacKinnon and Gregg, 2003](#); [Wijesekera et al.,](#)
 245 [1993](#)). It is noteworthy to mention that these parameterizations applied to CTD/LADCP
 246 data are able to reproduce observed levels of ϵ within a factor of two for conditions close
 247 to the GM79 model ([Gregg, 1989](#)), a semi-empirical model of oceanic internal waves far
 248 from generation and dissipation area.

249

250 *GM-based Gregg- Henyey- Polzin model*

251 The parameterization proposed by [Henyey et al. \(1986\)](#) and extensively tested by
 252 [Gregg \(1989\)](#) reads:

$$\epsilon_{G89} = 7 \times 10^{-10} \left(\frac{N^2}{N_0^2} \right) \left(\frac{S^4}{S_{GM}^4} \right) \quad (3)$$

253 where N_0 is the canonical GM buoyancy frequency, S is the shear of horizontal velocities
 254 and S_{GM} is the GM shear, with $S_{GM}^4 = 1.66 \times 10^{-10} (N^2/N_0^2)^2$. The shear, S , was first cal-
 255 culated in the spectral domain and then back-transformed to the physical domain after
 256 removing all wavelengths smaller than 16 m (Nyquist wavelength) and the buoyancy fre-
 257 quency N was averaged over 16 m for consistency. Data points with either $N^2 < 10^{-7} s^{-2}$
 258 and / or $S^2 < 10^{-7} s^{-2}$ were excluded from the computations to avoid spurious values
 259 affected by the noise level on N and / or S assuming a precision of $\sim 10^{-4} kgm^{-3}$ for
 260 density and of $\sim 10^{-2} ms^{-1}$ for velocity. Equation (3) is based upon the assumption of a
 261 constant shear to strain ratio equal to that of GM. [Polzin et al. \(1995\)](#) showed that this
 262 ratio, R_ω , was a function of the frequency content of the internal wave field. Thus, they
 263 introduced an additional factor to G89, $h(R_\omega) = 3(R_\omega + 1)/[2\sqrt{2}R_\omega\sqrt{(R_\omega - 1)}]$ (see as
 264 well [Kunze et al., 2006](#); [Gregg et al., 2003](#)). Additionally, a factor function of latitude
 265 was introduced by [Gregg et al. \(2003\)](#), leading to the most popular incarnation (e.g.,
 266 [Cuypers et al., 2012](#); [Pasquet et al., 2016](#)):

$$\epsilon_{GHP} = \frac{f \cosh^{-1}\left(\frac{N}{f}\right)}{f_{30} \cosh^{-1}\left(\frac{N_0}{f_{30}}\right)} h(R_\omega) \epsilon_{G89} \quad (4)$$

267 For the repeated stations, a time-mean density profile was calculated from which strain
 268 and buoyancy frequency were calculated and subsequently filtered using a 10-m mov-
 269 ing average and a mean $R_\omega = \langle S^2 \rangle / (\langle N^2 \rangle \langle \zeta_z^2 \rangle)$ was inferred. For the station S_4
 270 single profile, the isopycnal displacements were estimated from a reference stratification
 271 inferred from a 100-m moving average of N^2 . In all cases, regions of low stratification
 272 and low shear, $N^2 < 10^{-7} s^{-2}$ and/or $S^2 < 10^{-7} s^{-2}$, were excluded.

273 We also tested one of the most recent formulation of the previous parameterization in

274 which shear and strain variances are computed in spectral space using 320 m segments
 275 (e.g. [Kunze et al., 2006](#)), referred to as ϵ_{K06} . This method especially designed for deep
 276 profiles was extensively applied to infer the large scale structure of ϵ and K_z using CTD
 277 and LADCP data surveys (e.g., [Naveira Garabato et al., 2004](#); [Walter et al., 2005](#); [Kunze](#)
 278 [et al., 2006](#); [Huussen et al., 2012](#); [Waterman et al., 2013](#)). ϵ_{K06} provides an averaged es-
 279 timate of ϵ compared to ϵ_{GHP} . Details of the method and results for ϵ_{K06} are shown in
 280 the appendix.

281

282 *Narrow-band internal wave spectrum*

283 [MacKinnon and Gregg \(2005\)](#) proposed a formulation that applies to an internal wave
 284 field dominated by a low-mode wave. In this case, they found that the energy dissipation
 285 rate scales like the low-frequency shear: $\epsilon \sim (N/N_0)(S_{lf}/S_0)$, with S_{lf} the low mode
 286 shear. This scaling, originally developed for a coastal environment, was validated by
 287 [Xie et al. \(2013\)](#) in the deep Bay of Biscay in the presence of strong internal tides and a
 288 strong seasonal thermocline. Since our study region also exhibited a low wavenumber
 289 component in the background tidal shear, we followed [Xie et al. \(2013\)](#) and computed a
 290 modified MG formulation that reads:

$$\epsilon_{MG} = \epsilon_0 \left(\frac{N}{N_0} \right) \left(\frac{S}{S_0} \right) \quad (5)$$

291 with ϵ_0 is an adjustable parameter determined from VMP measurements equal to $2 \times$
 292 $10^{-10} \text{ W kg}^{-1}$, S is the vertical shear computed in spectral space, low-pass filtered with

293 1/16cpm upper bound for vertical wavenumbers, and with $S_0 = 3/3600 \text{ s}^{-1}$.

294

295 2.5 Vertical shear spectra

296 Vertical wavenumber shear spectra were computed for each LADCP profile and aver-
297 aged by station (Figure 3). For each horizontal velocity profile, a periodic signal was
298 constructed using symmetry properties (e.g. [Canuto et al., 1988](#); [Bouruet-Aubertot et al.,](#)
299 [1995](#)). The spectrum was computed using a rectangular window whose length equals
300 the periodic signal. For comparison, two GM shear spectra are shown in Figure 3: the
301 GM shear spectrum with its canonical shear variance and a GM spectrum fitted to the
302 observed shear variance, which was computed in spectral space up to $k_c = 1/100 \text{ cpm}$
303 (Figure 3, red and black dashed lines respectively). Shear spectra have a shape close
304 to the GM shape ([Garrett and Munk, 1975](#)) for all stations (Figure 3, black curve) and
305 roll-off beyond a critical wavenumber. The observed shear spectral level is an order of
306 magnitude larger than the GM level at all stations except at station S_4 in the Banda Sea,
307 which suggests that ϵ_{GHP} should better predict ϵ at station S_4 than at the other stations.
308 Note that a few peaks are present for stations S_1 and S_3 at small vertical wavenumbers.
309 The strong dominance of diurnal and semi-diurnal tidal frequencies in the baroclinic
310 signals plus the presence of peaks at low wavenumbers in the shear spectrum suggest
311 that the internal wave field is dominated by low mode internal tides. Such properties
312 are typical of the MG framework which gives an additional motivation to test the MG

parameterization. Note that we do not see any signature of a white noise characterized by a k_z^2 dependency in the shear spectra indicating that the noise level is well below the physical shear variance at all shown wavenumbers. Another issue discussed by Polzin et al. (2002) is a possible high wavenumber attenuation of the shear spectrum resulting from the LADCP processing. The fact that we observe a GM shape below k_c suggests that this attenuation is negligible here. Therefore we did not apply any spectral correction on the LADCP signal.

3 A CONTRASTED SPATIAL DISTRIBUTION OF INTERNAL TIDES AND DISSIPATION RATE

3.1 Spatial distribution of internal tide energy from a linear model

Several hot spots of internal tide generation are found in the Indonesian seas (Figure 2). The generating force exhibits very similar patterns for the two constituents K_1 and M_2 (Figures 2a, b). As expected, the largest values are found within straits and over the shelf slopes since these regions are both characterized by strong barotropic currents and significant slopes. The map of the generating force in the Halmahera Sea (Figure 2) gives evidence of the contrast between stations S_1 and S_3 , which are both located in generation areas (near-field), and station S_2 located further away in deeper waters (intermediate field). Station S_4 in the Banda Sea is far from any generation area (far-field)

331 while station S_5 in the Ombai Strait is in a generation area (near-field).

332

333 The linear internal tide model was applied to a section passing by stations S_1 , S_2 and
334 S_3 in the Halmahera Sea and to a section crossing the Ombai Strait. Since the barotropic
335 tidal flux at these stations is close to the direction of the modeled section (Figure 2), the
336 idealized 2D-simulations are expected to give a first-order view of the true internal tidal
337 field in this area. Internal tidal rays generated at a few topographic features undergo
338 successive reflections at the surface and at 300-600m, leading to an enhanced internal
339 tide signal almost uniformly along the section in the upper three hundred meters (Figure
340 4a, b). Deeper, below ~ 600 m depth, the variation in internal tide amplitude is striking
341 with strong currents near generation regions and weak currents elsewhere except locally
342 near the bottom. The linear model predicts large internal tide energy levels over the
343 entire water column at station S_3 and to a lesser extent at station S_1 , while large values
344 are confined within the upper four hundred meters at station S_2 located further away
345 from a generation area. Based on this pattern, we expect to observe a strong internal tide
346 signal in the velocity and density fields at those three stations. A strong tidal signal is
347 generated at station S_5 located near the sill of the Ombai Strait (Figure 4 b, d). There, the
348 modeled internal tide signal is confined at depth within a few hundreds meters above
349 the bottom where both M2 and K1 internal rays superimpose.

3.2 Spatial distribution of internal tide energy from observations

The vertical and horizontal distribution of internal tide energy was diagnosed from the CTD-LADCP stations. The four stations with repeated profiles over two semi-diurnal periods provided us with time-depth sections of meridional currents (Figure 5, left-hand panels). The meridional component of the total current reaches velocities up to 1.3 m s^{-1} , 0.7 m s^{-1} , 1 m s^{-1} and 1.4 m s^{-1} at stations S_1 , S_2 , S_3 and S_5 respectively. The strongest currents are observed in the Ombai Strait (S_5) and at the entrance of the Halmahera Sea (S_1) and to a lesser extent at the Southern passage of the Halmahera Sea (S_3). Currents are significantly weaker at station S_2 (and at station S_4 with a maximum value of 0.4 m s^{-1} , not shown). This station, located in a deeper area compared to stations S_1 and S_3 , is away from generation areas (Figure 1b). The tidal component of the currents is further evidenced by the perturbation of the baroclinic current, i.e. the baroclinic current minus its time average, typically over two M_2 periods (i.e. $\vec{v}' = \overrightarrow{v_{\text{bcl}}} - \langle \overrightarrow{v_{\text{bcl}}} \rangle$ with $\overrightarrow{v_{\text{bcl}}} = \vec{v} - 1/H \int_0^H \vec{v} dz$) (Figure 5, right-hand panels). All stations, except station S_2 , exhibit strong currents ($\sim 1 \text{ m s}^{-1}$) and large isopycnal displacements of a few hundred meters at depth. Semi-diurnal and diurnal periods are easily identified: at 600 m at station S_1 and around 500-800m at station S_3 for the semi-diurnal component, and at 100 m depth at station S_1 for the diurnal component. Vertical propagations are evidenced in some cases: downward phase propagation at stations S_2 and S_3 , both downward and upward phase propagation at stations S_1 and S_5 . The diurnal and semi-diurnal constituents contribute more than 58% to the total variance.

371 SADCP data collected in the Halmahera Sea along the section corresponding to the 2D
372 linear simulations show strong currents at station S_1 and to a lesser extent at station S_3 ,
373 and weak currents at station S_2 (Figure 6a). The SADCP time series at the stations better
374 highlights the contrast in current magnitudes between stations (Figure 6b). The contrast
375 in the vertical shear of horizontal velocities is less obvious, as a result of the fairly coarse,
376 15m, vertical resolution of the 75 kHz SADCP, but still evident (Figure 6c). The propa-
377 gation of sharp localised bands of strong shear, resembling that of internal tidal rays in
378 the model, is nicely evidenced in the time series of Figure 6c.

379

380 The linear internal tide model (Gerkema et al., 2004) is consistent with velocity and
381 density observations: a weak internal tide energy is found at station S_2 while larger ones
382 are found at stations S_1 , S_3 and S_5 (Figure 4, Figure 5.c and d, Figure 6). At the energetic
383 stations, S_1 , S_3 and S_5 , the topography is supercritical toward diurnal and semi-diurnal
384 tides (i.e. the topography is steeper than the internal tidal beams leading to both up and
385 down scattering), which corresponds to the 'tall topography' case with a tidal excursion
386 smaller than one (e.g., Legg and Huijts, 2006) that favors internal tide generation (Figure
387 4). If strong enough, the barotropic flow can locally trap baroclinic internal wave modes,
388 thus reinforcing nonlinearities in the vicinity of generation areas such as stations S_1 , S_3
389 and S_5 . Interestingly, this linear model gives a preliminary insight in the context despite
390 it ignores the three dimensional propagation of internal waves, non-linearities in the
391 dynamics and the impact of the barotropic current on internal wave propagation (e.g.
392 Lelong and Dunkerton, 1998a,b; Lelong and Kunze, 2013).

393 3.3 Contrasting profiles of turbulent kinetic energy dissipation rates

394 The largest ϵ are observed at stations S_1 and S_5 with intense turbulence throughout
 395 the water column (Figure 7, colored profiles). These large values of ϵ are most often
 396 correlated with large isopycnal displacements and strain at depth (Figures 7a, d, black
 397 lines) and occasionally with strong shear (Figures 7a, d, magenta background). Spots of
 398 large ϵ are observed at station S_3 with periods of weaker turbulence (especially for time
 399 within $[4 - 9]h$, Figure 7c). In contrast, ϵ is typically smaller by more than one order of
 400 magnitude at station S_2 compared with the other stations, which is consistent with the
 401 weaker amplitude both in shear and strain.

402 Time-averaged profiles of dissipation rates ϵ and of diapycnal diffusivity K_z highlight
 403 the contrast in small-scale turbulence between the stations (Figure 8a, b). The largest ϵ
 404 are observed close to internal tide generation areas (stations S_1 , S_3 and S_5). The depth-
 405 averaged ϵ reached $9.8 \times 10^{-6} W kg^{-1}$ at station S_5 in the Ombai Strait, $4.9 \times 10^{-7} W kg^{-1}$
 406 at station S_1 and $2.8 \times 10^{-7} W kg^{-1}$ at station S_3 in the Halmahera Sea. In contrast, far
 407 from generation areas, in the Banda Sea at station S_4 , ϵ is smaller by several orders of
 408 magnitude below 100 m depth. Eventually, a few tens of kilometers away from genera-
 409 tion areas, an intermediate depth-averaged ϵ of $9 \times 10^{-9} W kg^{-1}$ is obtained at station
 410 S_2 (see Table 2). Averaging ϵ over the thermocline instead of the full-depth decreases
 411 the range of variations to a factor of 4 between the stations within straits ($S_1 > S_5 >$
 412 S_3), and to a factor of 2 between stations S_2 and S_3 (see Table 3). These variations of
 413 ϵ , weaker in the thermocline than at depth, are consistent with the linear tidal model

414 that shows much larger tidal currents in the thermocline than at depth. Interestingly, we
 415 note an increase in ϵ in the bottom 100 m (e.g. Figure 8a, station S_2), with values up to
 416 $\sim 10^{-8} \text{ W kg}^{-1}$, which might be a signature of the stratified bottom boundary layer (e.g.,
 417 [St Laurent and Thurnherr, 2007](#)).

418

419 As with ϵ , time-averaged profiles of K_z show that the largest values are located at
 420 stations S_1 , S_5 and S_3 , and the smallest at station S_4 (Figure 8b). The contrast is strik-
 421 ing between the intense mixing within passages, with a depth- and time-averaged K_z of
 422 $1.9 \times 10^{-3} \text{ m}^2 \text{ s}^{-1}$, $9.4 \times 10^{-4} \text{ m}^2 \text{ s}^{-1}$ and $3.7 \times 10^{-4} \text{ m}^2 \text{ s}^{-1}$ for stations S_5 , S_1 and S_3 respec-
 423 tively, and that of the Banda Sea located away from any generation area with a K_z of
 424 only $0.12 \times 10^{-4} \text{ m}^2 \text{ s}^{-1}$. In the thermocline, mean K_z values range from $1.8 \times 10^{-5} \text{ m}^2 \text{ s}^{-1}$
 425 at station S_4 in the Banda Sea to $1.7 \times 10^{-4} \text{ m}^2 \text{ s}^{-1}$ at station S_1 in the northern Halma-
 426 hera passage. In the thermocline of the Halmahera Sea (stations S_1 , S_2 and S_3), mean
 427 K_z values only vary within a factor of 10, thus following the homogeneity in the mean ϵ .
 428 Statistics of ϵ and K_z are summarized in Tables 2 and 3. The Osborn formulation of K_z
 429 is shown for comparison in Figure 8c. The estimates differ by two orders of magnitude
 430 at depth where turbulence intensity is strong, up to 10^7 . This points out the sensitivity
 431 of mixing estimates of water masses depending on the K_z parameterization in regions of
 432 strong turbulence intensity as outlined by [Shih et al. \(2005\)](#).

433

434 As previously mentioned, the turbulence intensity is a relevant and important param-
 435 eter to characterize the dynamics and the regime of turbulence, especially since turbu-
 436 lence is strongly intermittent and spatially heterogenous. The turbulence intensity, I

437 (Eq.(2)), associated with the repeated profiles at each station were calculated and aver-
 438 aged in time (Figure 9). Vertical profiles of the percentage of occurrences of $I \leq 1000$
 439 were calculated (Figure 9, red lines). I is always smaller than 1000 for the single profile
 440 of station S_4 except in the upper 100 m. In contrast, station-mean I -values are in the
 441 strongly energetic regime, $I > 1000$, for stations S_1 and S_5 , except in the upper 100 m
 442 and 200 m, respectively. Station S_3 shows a region of moderate station-mean I -value,
 443 of the order of 500, in the upper 300 m. Then strongly turbulent regimes increase from
 444 about 10 – 30% above the 300 m transition depth to 80% below. Station S_2 mean I -values
 445 are typically within $[\sim 100; \sim 1000]$ except in the last hundred meters where strongly
 446 turbulent regime prevails.

447

448 We next examine whether these variations in I are consistent with that of the station-
 449 mean profiles of baroclinic tidal energy (kinetic and available potential). Tidal energy is
 450 the largest at stations S_1 and S_5 , intermediate at station S_3 , and the smallest at station S_2 .
 451 This evolution is consistent with the overall variations of ϵ at the different stations. A
 452 more detailed comparison reveals that the contrast between stations evolves as a function
 453 of depth (Figure 10). In the first hundred meters, the tidal energy is of the same order of
 454 magnitude for all stations, consistently with ϵ (Figure 8a). Deeper, there is an increasing
 455 contrast between station S_2 and the three others: both ϵ and the tidal energy decrease
 456 significantly between 350 and 800 m at station S_2 . Eventually, for the deepest levels,
 457 there is an increase in tidal energy that is also correlated with that of ϵ . At the other
 458 stations, a correlation between ϵ and E_t is obtained below 300 m at station S_1 , and locally
 459 around 700 m depth at station S_5 . In some cases, when variations of ϵ are not correlated

460 with those of tidal energy, for instance at station S_3 between ~ 300 m and ~ 700 m, they
461 are correlated with the shear (non tidal). Note that processes other than internal tides
462 such as internal solitary waves might possibly come into play here, especially within
463 passages where huge isopycnal displacements are observed as for stations S_1 , S_3 in the
464 Halmahera Sea and station S_5 in the Ombai strait.

465 4 LOOKING FOR A FINESCALE PARAMETERIZATION OF IN- 466 TERNAL TIDAL MIXING

467 4.1 Test of finescale parameterizations

468 In this set of stations with contrasting dissipation rates and turbulence intensities, finescale
469 parameterizations, ϵ_{GHP} and ϵ_{MG} , are compared against VMP measurements (Figure 11).
470 ϵ_{GHP} reproduces reasonably well ϵ_{VMP} at station S_4 (Figure 11d) which is located far
471 from any internal tide generation area and with a weak atmospheric forcing. As a result
472 the shear level is close to the GM value and nonlinear interactions are weak, falling into
473 the domain of validity of the GHP parameterization. At the other stations, where the in-
474 ternal tides are more energetic, ϵ_{GHP} strongly underestimates ϵ_{VMP} by at least one order
475 of magnitude. This is somewhat expected since ϵ_{GHP} is meant for an internal wave field
476 close to GM levels, while, at these stations, observed shear levels are ten-fold larger than

477 GM levels (Figure 3).

478

479 Contrastingly, ϵ_{MG} better predicts ϵ_{VMP} when the shear level is significantly higher
 480 than the GM value. It provides a relevant estimate at station S_2 (Figure 11b) and in the
 481 upper part of the water column at stations S_1 , S_3 and S_5 (Figure 11a, c, e).

482 Interestingly, regions where ϵ_{MG} better fits ϵ_{VMP} seem related to regions of moder-
 483 ate turbulence intensities. In order to determine if a threshold value of I bounds the
 484 domain where ϵ_{MG} is a relevant estimate of ϵ_{VMP} , ϵ_{MG} is compared with ϵ_{VMP} as a
 485 function of turbulence intensities (Figure 12). There is a striking difference between
 486 station S_2 , marked by moderate turbulence intensities for which ϵ_{MG} is fairly relevant,
 487 and stations S_1 , S_3 , and S_5 marked by strong turbulence intensities for which ϵ_{MG} clearly
 488 underestimates ϵ_{VMP} . I is typically smaller than 1000 at station S_2 over most of the water
 489 column. At the energetic stations, S_1 , S_3 and S_5 , I is also smaller than 1000 in the first
 490 few hundred meters and sharply increases below (see for instance the transition around
 491 300 m at station S_3 , Figure 9c). ϵ_{MG} starts to deviate from ϵ_{VMP} around this transition
 492 in I values. ϵ_{MG} largely underestimates ϵ_{VMP} at depth where strong turbulent regime
 493 prevails ($I > 1000$), which suggests that either strong non-linear wave-wave interactions
 494 or other processes than instabilities related to internal waves come into play. Finally, at
 495 station S_4 for which $I < 100$, ϵ_{MG} overestimates ϵ_{VMP} (Figure 11d). Thus, this data set
 496 suggests that for weakly turbulent regime ($I < 100$), ϵ_{GHP} is the most appropriate; for
 497 moderate turbulent regime ($100 < I < 1000$), ϵ_{MG} is the most appropriate; while for
 498 strong turbulent regime ($I > 1000$) none of these parameterizations are relevant.

499

500 Turbulence is often characterized by stabilizing (stratification, N) and destabilizing
 501 (vertical velocity shear, S) forces. In order to get more physical insight in the parameter-
 502 ization of ϵ , we next compare their properties to those of ϵ_{VMP} in (S^2, N^2) space (Figure
 503 13a-d). If turbulence is shear-induced, large dissipation rates are expected in regions
 504 of low Richardson number, $Ri = N^2/S^2$. The following regions where either ϵ_{GHP} or
 505 ϵ_{MG} provide a reasonable estimate of ϵ_{VMP} according to the station-mean dissipation
 506 rate profiles were selected (Figure 11): the whole profiles of ϵ_{MG} at station S_2 and ϵ_{GHP}
 507 at station S_4 and the upper 300 m of ϵ_{MG} at station S_3 . At station S_2 , the largest values
 508 of ϵ_{VMP} are obtained for large shear and strong stratification of the thermocline (Fig-
 509 ure 13a). ϵ_{MG} is able to reproduce this observed property (Figure 13d). Similarly, the
 510 pattern of ϵ_{MG} is close to that of ϵ_{VMP} in the first 300 m at station S_3 (Figure 13b and
 511 e). At station S_4 in the Banda Sea, the pattern of ϵ_{VMP} with low values in the regions
 512 of strongest shear and stratification and large values for low Ri is well reproduced by
 513 ϵ_{GHP} (Figure 13c and f). This shows the fundamental difference between ϵ dependency
 514 in (N^2, S^2) space as a function of turbulence intensity (i.e. weakly nonlinear interactions
 515 for $I < 100$ and more nonlinear regimes for $100 < I < 1000$) and the relevance of ϵ_{GHP}
 516 and ϵ_{MG} respectively to reproduce this pattern.

517 4.2 Estimate of turbulent kinetic energy dissipation rate in regions of strong turbulent 518 intensity

519 Finescale parameterizations are used to estimate the dissipation rates based on the prop-
520 erties of the internal wavefield with the assumption that internal waves weakly interact.
521 Such parameterizations are expected to be relevant for weakly to moderately strong non-
522 linear interactions, but not necessarily for more non-linear wave dynamics, or stratified
523 turbulence. Furthermore, the finescale parameterisations assume that the velocity shear
524 and strain are indeed representative of the internal wave field. To get insights in the dy-
525 namical regime resolved with CTD/LADCP measurements, we look at the length scales
526 that bound the inertial range of 3D turbulence, namely the Ozmidov scale $L_O = \sqrt{\epsilon/N^3}$
527 and the Kolmogorov scale $L_K = (\nu^3/\epsilon)^{1/4}$ (Figure 14). L_O defines the vertical displace-
528 ment resulting from the full conversion of the turbulent kinetic energy into available po-
529 tential energy, it corresponds to the maximum scale of eddies within the inertial range
530 while L_K is the scale at which the turbulent kinetic energy is dissipated into heat. The
531 Ozmidov scale varies widely from a few cm up to ~ 100 m. The smallest scales are
532 reached in the thermocline and the largest at the deepest depths. The vertical LADCP
533 bin size, $\Delta z = 8$ m, is shown for comparison. When $L_O > \Delta z$, LADCP measurements fall
534 in the inertial range in an averaged sense. Thus, a velocity difference calculated over a
535 scale Δz , $\delta v = |\overrightarrow{v(z + \Delta z)} - \overrightarrow{v(z)}|$, is expected to follow the Kolmogorov scaling only when
536 $L_O > \Delta z$. A significant part of stations S_1 , S_3 and S_5 profiles fall into the inertial range
537 since $L_O > \Delta z$ for height above the bottom smaller than 600 m, 400 m and 800 m respec-

538 tively. In this range, the Kolmogorov theory predicts that the dissipation rate is given by
539 $\epsilon_{\text{IR}} = \delta v^3/l$ within a factor of order 1, where δv is the velocity difference at scale l (e.g.,
540 [Tennekes and Lumley, 1972](#)). A similar approach is adopted in the large eddy method,
541 LEM, which is based on a scaling of the turbulent kinetic energy equation ([Taylor, 1935](#))
542 using a pragmatic approach to determine the ‘transition’ scale between fine-scale and
543 turbulent motions and infer the turbulent kinetic energy (e.g. [Moum, 1996](#); [Peters et al.,](#)
544 [1995](#); [Beaird et al., 2012](#)). Using $l = \Delta z = 8$ m, ϵ_{IR} was compared with ϵ_{VMP} to check
545 its relevance (Figure 15). There is generally a relatively good correspondance between
546 ϵ_{VMP} and ϵ_{IR} provided that the averaged Ozmidov scale is larger than ~ 8 m. Several
547 reasons possibly contribute to errors in the estimate of ϵ_{IR} . Firstly, the assumption of 3D
548 homogeneous and isotropic turbulence is not necessarily fulfilled. If not this will impact
549 both the estimate of ϵ_{VMP} , inferred from the components of the vertical shear only, and
550 the rate of energy transfers inferred from vertical velocity differences. Secondly, in some
551 cases, the time averaged values of ϵ_{VMP} and ϵ_{IR} , that take into account between 5 to 12
552 profiles, are strongly influenced by 1 or 2 very large values such as at station S₅. The
553 ability of ϵ_{IR} to predict ϵ_{VMP} within a factor of 10, 5 and 2 was computed for regions
554 such that $L_O > 8$ m (Table 4). In all cases, except at station S₂, more than 75% of the ratio
555 $\epsilon_{\text{IR}}/\epsilon_{\text{VMP}}$ falls within a factor of 2.

556

557 5 SUMMARY AND DISCUSSION

558 Microstructure measurements gave evidence of the contrast between the very large dis-
559 sipation rates encountered in passages and those, still large but smaller, measured in
560 deeper regions further away from generation areas of internal tides (see as well Koch-
561 Larrouy et al., 2015). Depth averaged dissipation rates varied by 4 orders of magnitude
562 over the whole water column and by 2 orders of magnitude in the thermocline. This
563 distribution was explained by the presence of strong barotropic and baroclinic tidal cur-
564 rents within passages, whereas the internal tidal signal is more confined within the
565 thermocline for stations further away from any generation area. Note that baroclinic
566 near-inertial waves may also contribute to the enhanced internal wave signal in the up-
567 per few hundred meters as previously evidenced by Alford et al. (1999) in the Banda Sea.
568 Their cruise was held in October, a few weeks after the strong summer monsoon winds
569 that led to the generation of the observed baroclinic near-inertial wave. The INDOMIX
570 cruise was held in July during the strong summer monsoon winds period that favors
571 the generation of energetic baroclinic near-inertial waves. It is hypothesized that the en-
572 ergetic baroclinic near-inertial waves, that may have been induced by the strong winds
573 observed during the cruise in the Banda Sea and in the Ombai strait, were not sampled
574 since their propagation at depth is typically observed within a few weeks after the strong
575 summer wind period (e.g., Alford et al., 1999). In any case, it was not possible to char-
576 acterize baroclinic near-inertial waves with our one day measurements since the inertial
577 period was at least of 3.5 days. Maximum K_z values in the thermocline, where most

578 water mass transformations occur, ranged from $2 \times 10^{-3} \text{ m}^2 \text{ s}^{-1}$ down to $7 \times 10^{-4} \text{ m}^2 \text{ s}^{-1}$,
579 which is consistent with integrated estimates from water mass transformations (Ffield
580 and Gordon, 1992). In regions of strong turbulent intensity, the Osborn parameterization
581 overestimated the mean K_z by a factor of ~ 50 compared to the Bouffard parameteriza-
582 tion as mixing efficiency decreases with increasing turbulent intensity. The consequence
583 on watermass transformation should be significant in the Indonesian Seas, as already
584 pointed out in a numerical study at global scale by De Lavergne et al. (2016a) and more
585 specifically for the Antarctic Bottom Water by De Lavergne et al. (2016b).

586 Turbulence intensity, indicative of non-linearities in the internal wave field, ranged
587 from ~ 7 up to 10^7 . Hence, this dataset shows that different processes at the origin
588 of the energy cascade toward small scales are expected depending on the regime of tur-
589 bulence intensity: in the weakly turbulent regime ($I < 100$), the internal wave field is
590 close to GM and marked by weakly non linear interactions; in the moderately turbulent
591 regime ($100 < I < 1000$), an energetic dominant internal tide is found with an inter-
592 nal wave energy level ten-fold larger than the GM level; in the strong turbulent regime
593 ($I > 1000$) that prevails near sills, non-linear waves, convectively unstable, are expected
594 as observed by van Haren et al. (2015), leading to direct energy transfers toward small-
595 scales (e.g. Lelong and Dunkerton, 1998a,b). The presence of large barotropic currents
596 also suggested possible wave trapping of high baroclinic modes with upstream phase
597 propagation. However the exact nature of the processes involved was however difficult
598 to assess as we lack cross-sill measurements.

599

600 In this very specific situation of highly variable internal wave energy levels, two
601 fine-scale parameterizations were tested: the Gregg-Henyey-Polzin parameterization de-
602 signed for internal wave fields close to GM, and that proposed by MacKinnon and Gregg
603 (2003) which was validated for non GM internal wave fields (e.g. Xie et al., 2013). Far
604 from generation areas, in the ‘far-field’ region characterized by shear levels close to
605 the GM level and weak turbulence intensities, ϵ_{GHP} and ϵ_{K06} formulations of the Gregg-
606 Henyey-Polzin parameterization provided a relevant estimate of ϵ . In the Halmahera
607 Sea and the Ombai Strait where the shear level is larger, MG parameterization provided
608 a relevant estimate of ϵ for moderate turbulence intensities. In the strongly nonlinear
609 regimes, for which none of these parameterizations applied, stratification effects are
610 negligible and the Kolmogorov scaling of epsilon inferred from velocity differences,
611 ϵ_{IR} , provided a relevant estimate of the dissipation rate when the vertical resolution of
612 CTD/LADCP measurements fell into the inertial range domain. Our results are consis-
613 tent with previous findings based on a simple ϵ scaling function of the turbulent kinetic
614 energy, i.e. the large eddy method, LEM, which was found of relevance provided that
615 scales smaller than overturning scales are resolved (e.g., Moum, 1996; Peters et al., 1995;
616 Beaird et al., 2012).

617 Some guidelines for a practical procedure to infer finescale estimates of ϵ can be drawn
618 from this study though more work with a larger dataset would be required for refined
619 conclusions. This procedure requires three stages. Firstly, the comparison with the GM
620 shear spectra should be performed: whether the observed shear spectra are close both
621 in shape and level to the GM shear spectra or not will determine if the Gregg-Henyey-
622 Polzin parameterization applies. If these conditions are not fulfilled, but if instead a few

623 low modes are observed, the MG parameterization should apply provided that the shear
624 level remains within a factor of 10 of the GM shear level. For the strongest turbulent
625 regimes, typically encountered near generation areas for internal tides, the Kolmogorov
626 scaling (ϵ_{IR}) appears to be the most relevant provided that part of the vertical scales
627 of velocity measurements fall within the inertial subrange, which can be inferred from
628 Thorpe scales.

629 This dataset raises the question of the scaling of the dissipation rate for more strongly
630 non-linear regimes that correspond to turbulence intensities larger than ~ 1000 . Several
631 studies focused on the parameterization of the dissipation rate over sills where the inter-
632 nal tide regime dominates (e.g., [Klymak et al., 2010](#); [Legg and Huijts, 2006](#)). For instance
633 [Klymak et al. \(2010\)](#) proposed an estimate of dissipation rate from the barotropic tidal
634 power conversion into trapped baroclinic modes in the case of a knife-edge topography
635 [Llewellyn Smith and Young \(2003\)](#). This parameterization was tested within the Ombai
636 strait but this seemed a too ambitious goal owing to the lack of measurements across
637 the sill. A dedicated survey with fine- and micro-structure measurements across the
638 passage, including the main generation area at the sill, would enable validation of a pa-
639 rameterization of dissipation rate and to compute the energy flux of trapped baroclinic
640 modes.

641

642 Acknowledgment

643 We thank the chief scientist, Ariane Koch-Larrouy, and H el ene Leau from IPEV for their
644 support during the cruise and Robert Molcard for his numerous advices. We warmly
645 acknowledge the assistance of the crew of the french research vessel Marion-Dufresne,

646 during the deployment of the VMP. We thank Claudie Marec and Jacques Grelet for
 647 their technical support for the CTD-LADCP and for post-processing these data as well as
 648 Annie Kartavtseff for processing the SADCP data. This work was financially supported
 649 by LEFE-IDAO and additional funding by LOCEAN. The microstructure profiler was
 650 funded by the French Agence Nationale de la Recherche (ANR) through the ANR-JC05-
 651 50690 grant and part of the functioning expenses by the French Institute for Marine
 652 Science (IFREMER). The INDOMIX cruise is a collaborative research between France
 653 and Indonesia. Agus Atmadipoera was funded in part by a grant from the Ministry
 654 Education National (DIKTI), through contract 591.11/I3/11/PL/2010.

655 6 APPENDIX: TEST OF ONE OF THE KUNZE ET AL (2006)

656 PARAMETERIZATION

657 We applied the procedure described by [Kunze et al. \(2006\)](#) with additional details pro-
 658 vided in [Pasquet et al. \(2016\)](#). The vertical eddy diffusivity is inferred from the shear
 659 and strain variances computed using a spectral method upon vertical segments of 320 m
 660 for the shear and 256m for the strain with an overlap of 160 m. Following [Kunze et al.](#)
 661 [\(2006\)](#) we first compute diapycnal diffusivity, K_{K06} which is given by:

$$662 \quad K_{K06} = K_0 \frac{\langle S^2 \rangle^2}{\langle S^2 \rangle_{GM}^2} j(f/N)h(R_\omega) \quad (6)$$

663 S^2 is the shear variance which is obtained by integrating the shear spectrum on the verti-
 664 cal wavenumber interval $[\frac{2\pi}{320} \text{ rad m}^{-1}; k_c]$ where k_c is equal to the minimum wavenum-
 665 ber between the default value $\frac{2\pi}{16} \text{ rad m}^{-1}$ and the wavenumber at which the signal to
 666 noise ratio is equal to 5 (see [Pasquet et al. \(2016\)](#) for details); the other terms are defined
 667 as follows:

$$668 \quad K_0 = 5 \times 10^{-6} \text{ m}^2 \cdot \text{s}^{-1} \quad (7)$$

$$669 \quad j(f/N) = \frac{f \cosh^{-1}(\bar{N}/f)}{f_{30} \cosh^{-1}(N_0/f_{30})} \quad (8)$$

670 f is the Coriolis parameter, f_{30} is the Coriolis value at 30N, (8) takes into account the
 671 variation with latitude ([Gregg et al., 2003](#)) and \bar{N} is the buoyancy frequency averaged
 672 over the 320 m length segment. Note that we have taken into account in our calculation
 673 the corrections of LADCP shear proposed by Polzin et al. (2002) and Thurnherr et al.
 674 (2012) (see [Pasquet et al., 2016](#), for further details).

675 Dissipation rate is then inferred as:

$$676 \quad \epsilon_{K06} = 5K_{K06}\bar{N}^2 \quad (9)$$

677 ϵ_{K06} was compared at all stations with ϵ_{vmp} which was averaged over the computa-
 678 tions intervals of ϵ_{K06} for consistency (Figure 16). ϵ_{K06} predicts well dissipation rates at
 679 station S_4 , with a mean $\epsilon_{K06}/\epsilon_{vmp}$ ratio equal to 2, while it underestimates ϵ_{vmp} at all the
 680 other stations with a mean $\epsilon_{K06}/\epsilon_{vmp}$ ratio varying from 3×10^{-4} at station S_1 to 7×10^{-2}
 681 at station S_2 . These results show a close similarity between ϵ_{K06} and ϵ_{GHP} namely a good
 682 agreement with ϵ_{vmp} when the shear level is comparable to the GM value. A closer com-
 683 parison between these two formulations that mainly differ in the computation method is

684 displayed in Figure 16 with ϵ_{GHP} averaged over the 320 m computation interval of ϵ_{K06} .
685 The two formulations are consistent at all stations with a mean ratio between ϵ_{K06} and
686 ϵ_{GHP} within the range [0.2; 2]. The fact that the range of variation is slightly larger than a
687 factor of two results from the difference in computation methods. The ϵ_{K06} computation
688 using 320 m depth intervals provides a smoother estimate compared to the original ϵ_{GHP} .
689 The ϵ_{K06} computation based on spectral variance computation over large depth intervals
690 is especially relevant when a single profile is available by increasing the statistics. When
691 repeated profiles are available at the same location, the use of ϵ_{GHP} allows an ϵ estimate
692 at higher vertical resolution.

693 LIST OF FIGURES

- 694 Figure 1 Bathymetry of the Indonesian seas (Smith and Sandwell, [http :](http://topex.ucsd.edu/marine_topo/)
695 [//topex.ucsd.edu/marine_topo/](http://topex.ucsd.edu/marine_topo/)). The three main areas of inter-
696 est are labelled and stations are indicated by red circles. 43
- 697 Figure 2 Baroclinic tide generating force inferred from the TPXO 7.2 model
698 for (a) diurnal K_1 and (b) semi-diurnal M_2 baroclinic tides (10^{-4}m s^{-2});
699 stations are indicated by red circles, except for the single profile
700 station S_4 with a white disk added; the direction of the barotropic
701 tidal flux for each constituent is shown in red and its modulus
702 is proportional to the radius of the outer red circle of the yellow
703 disks centered at the station location with reference circle taken
704 at station S_2 , where the barotropic tidal flux is of $110 \text{m}^2 \text{s}^{-1}$ for
705 the diurnal frequency and of $140 \text{m}^2 \text{s}^{-1}$ for the semi-diurnal fre-
706 quency. 44
- 707 Figure 3 Observed shear spectra from LADCP (blue), canonical GM spectra
708 (red) and GM spectra fitted to the observed shear variance (black).
709 Ratios between observed and canonical GM shear variances com-
710 puted up to $k_c = 1/100 \text{cpm}$ are equal to: 17, 13, 15, 18 and 1.2
711 for stations S_1, S_2, S_3, S_5 and S_4 . The 95% confidence interval is
712 shown with an error bar. 45

- 731 **Figure 6** Vertical section of the modulus of the horizontal current magni-
732 tudes in m s^{-1} from SADCP data passing through the three sta-
733 tions of the Halmahera Sea (a). SADCP data were time averaged
734 over two M2 tidal cycles at the location of the three stations in (a).
735 Vertical sections of time series at stations S_1 , S_2 and S_3 of the mod-
736 ulus of the horizontal current and of its vertical shear are shown
737 in (b) and (c). 48
- 738 **Figure 7** Dissipation rate from velocity microstructure (color log-scale, units
739 in W kg^{-1}), vertical shear of horizontal velocities from ship-ADCP
740 (magenta colorscale, from 0 to 0.03 s^{-1} , gray when no data) and
741 isopycnals inferred from sorted density profiles (same black con-
742 tours as in Figure 5) as a function of time for the stations S_1 - S_3
743 in the Halmahera Sea and S_5 in the Ombai Strait. Black vertical
744 dotted lines denote the time location of the CTD casts. Note that
745 the maximum depth of each subplot corresponds to the maximum
746 station depth. 49

| | | | |
|-----|-----------|---|----|
| 747 | Figure 8 | Time-mean profiles of energy dissipation rate ϵ , (a), vertical dif- | |
| 748 | | fusion coefficient K_z , (b), vertical diffusion coefficient based on | |
| 749 | | Osborn method $K_{z_{Osborn}}$, (c), and buoyancy frequency square N^2 , | |
| 750 | | (d), for the 5 stations. Note that a 10-meter moving average has | |
| 751 | | been applied for better vizualisation. Maximum values and stan- | |
| 752 | | dard deviations are listed in Tables 2 and 3. The bottom depth of | |
| 753 | | the stations is indicated in (d) by an horizontal colored line except | |
| 754 | | for station S_4 whose bottom depth is 4750 m. | 50 |
| 755 | Figure 9 | Time-averaged profiles of turbulence intensity (blue) for stations | |
| 756 | | S_1 , S_2 , S_3 , and S_5 and percentage of occurrence of $I < 1000$ (red). | |
| 757 | | The turbulence intensity profile for the single profile of station S_4 | |
| 758 | | plotted is shown. All curves have been smoothed using a 10-m | |
| 759 | | moving average for clarity. | 51 |
| 760 | Figure 10 | Mean profiles of total baroclinic tidal energy for the 4 stations | |
| 761 | | (diurnal+semi-diurnal). The bottom depth of the stations is indi- | |
| 762 | | cated by an horizontal colored line. | 52 |
| 763 | Figure 11 | Mean profiles of ϵ derived from finescale parameterizations and | |
| 764 | | from VMP measurements are compared at each station. The bot- | |
| 765 | | tom depth of the stations is indicated by a black horizontal line | |
| 766 | | except for station S_4 | 53 |

- 767 Figure 12 Mean profiles of ϵ derived from MG finescale parameterization,
768 ϵ_{MG} , for stations S_1 , S_2 , S_3 and S_5 , as a function of ϵ_{VMP} with
769 turbulence intensity displayed in color. Black lines (resp. blue)
770 denote a perfect agreement (resp. a factor of 10) between blue
771 ϵ_{MG} and ϵ_{VMP} 54
- 772 Figure 13 Bin-averaged dissipation rate (first row: ϵ_{VMP} ; second row: pa-
773 rameterization) as a function of shear and stratification: station S_2
774 (a) and (d), upper 300 m of station S_3 (b) and (e), station S_4 (c) and
775 (f). Critical Richardson number, $Ri = 0.25$, is shown as a black
776 dashed line. Note all CTD and LADCP profiles were included
777 for the parameterized ϵ and not only those performed when VMP
778 profiles were available. 55
- 779 Figure 14 Mean profiles of Ozmidov and Kolmogorov scales as a function of
780 depth for station S_1 (a), station S_2 (b), station S_3 (c) and station S_5
781 (d). The red dotted line denotes the vertical LADCP bin size (8 m). 56
- 782 Figure 15 Mean profile of ϵ_{VMP} (red curve) and ϵ_{IR} (black curve) as a func-
783 tion of depth for station S_1 (a), station S_2 (b), station S_3 (c) and
784 station S_5 (d). A 10-m moving average was applied to the mean
785 profiles of ϵ_{VMP} and ϵ_{IR} for clarity. Gray shaded regions indicate
786 depth intervals where ϵ_{IR} is not relevant (mean Ozmidov scale
787 smaller than 8 m). 57

| | | | |
|-----|-----------|---|----|
| 788 | Figure 16 | Mean profiles of ϵ derived from the Kunze et al. (2006) finescale parameterization at all stations, ϵ_{K06} is shown in blue, and $\langle \epsilon_{VMP} \rangle$ averaged over the 320 m computation intervals with an overlap of 160 m in red. $\langle \epsilon_{GHP} \rangle$ is shown as well for comparison. The bottom depth of the stations is indicated by a black horizontal line except for station S_4 | 58 |
|-----|-----------|---|----|

794 LIST OF TABLES

| | | | |
|-----|---------|--|----|
| 795 | Table 1 | Position of the stations, depths and number of VMP profiles, maximum and mean of barotropic velocity modulus. | 59 |
| 796 | | | |
| 797 | Table 2 | Mean, standard deviation and extrema of ϵ_{VMP} ($W\ kg^{-1}$) and of K_z ($m^2\ s^{-1}$). The average and standard deviation, σ , were first computed over time and next averaged over depth. The average of Kz_{Osborn} is displayed for comparison. | 60 |
| 798 | | | |
| 799 | | | |
| 800 | | | |
| 801 | Table 3 | Same as Table 2 but within the thermocline. The depth range for thermocline statistics is [50 – 200]m except at station S_4 with a [50 – 120]m depth range. | 61 |
| 802 | | | |
| 803 | | | |
| 804 | Table 4 | Percentage of agreement within a factor of 10 (1st column), 5 (2nd column) and 2 (3rd column) of ϵ_{IR} for data such that $L_O > 8\ m$. . . | 62 |
| 805 | | | |

806 **7** FIGURES

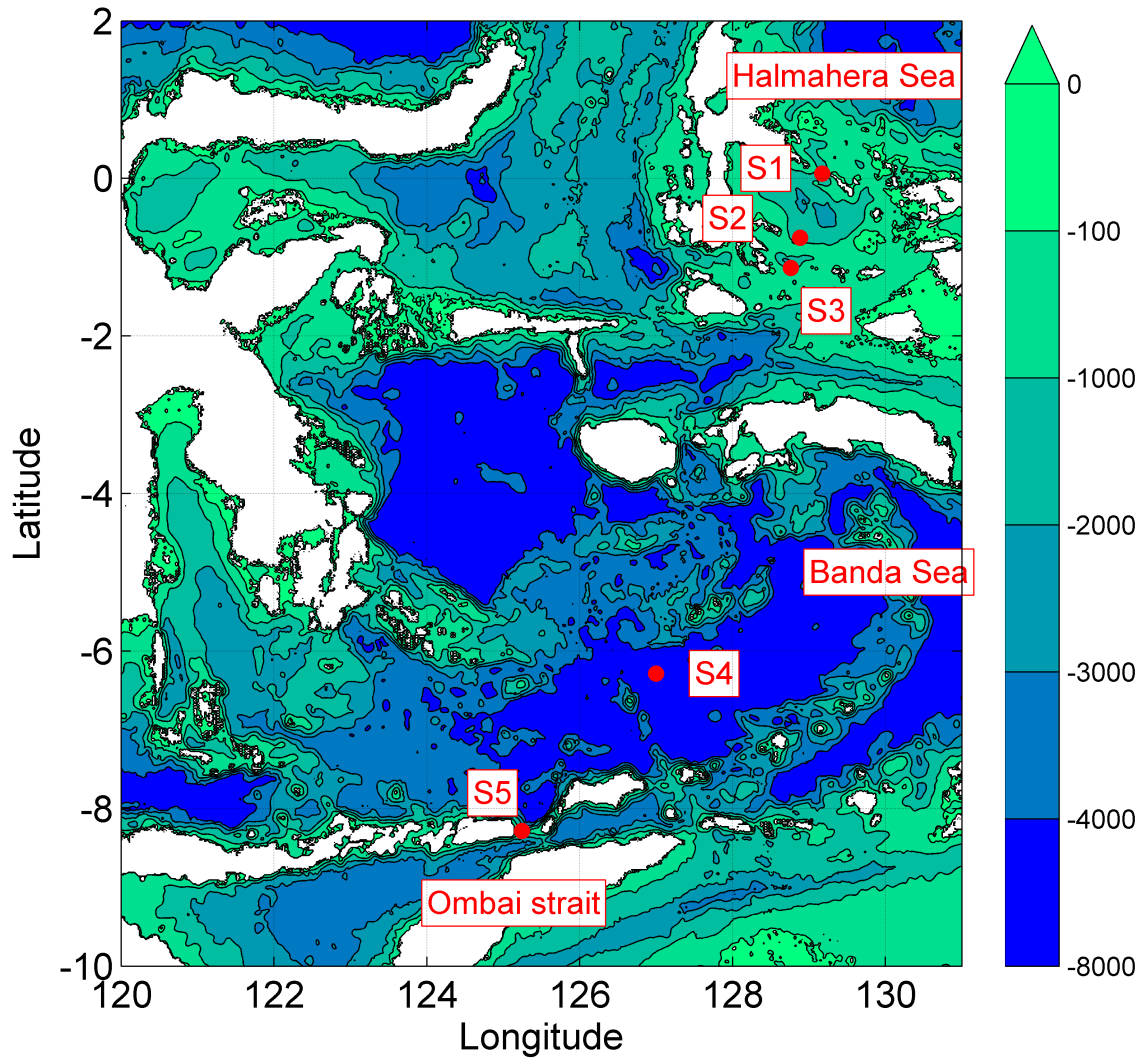


Figure 1: Bathymetry of the Indonesian seas (Smith and Sandwell, http://topex.ucsd.edu/marine_topo/). The three main areas of interest are labelled and stations are indicated by red circles.

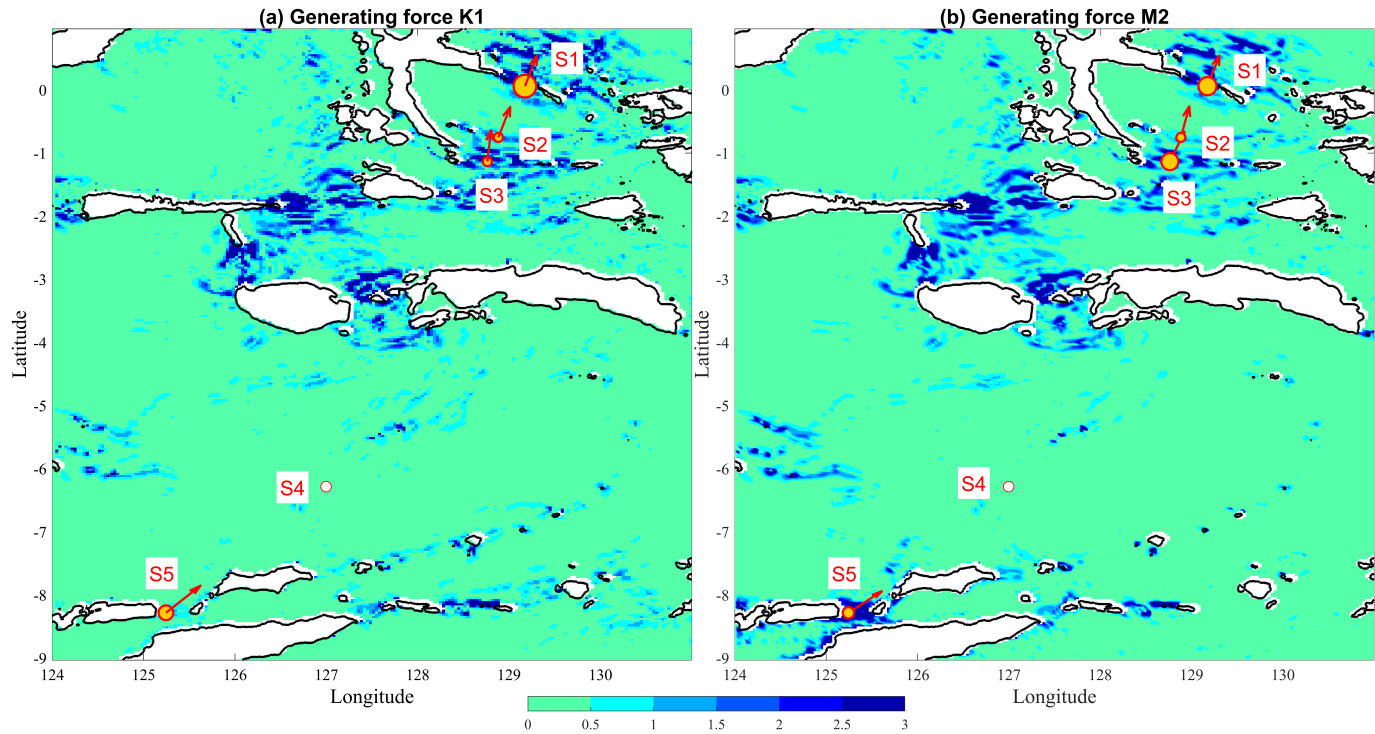


Figure 2: Baroclinic tide generating force inferred from the TPXO 7.2 model for (a) diurnal K_1 and (b) semi-diurnal M_2 baroclinic tides (10^{-4}m s^{-2}); stations are indicated by red circles, except for the single profile station S_4 with a white disk added; the direction of the barotropic tidal flux for each constituent is shown in red and its modulus is proportional to the radius of the outer red circle of the yellow disks centered at the station location with reference circle taken at station S_2 , where the barotropic tidal flux is of $110 \text{m}^2 \text{s}^{-1}$ for the diurnal frequency and of $140 \text{m}^2 \text{s}^{-1}$ for the semi-diurnal frequency.

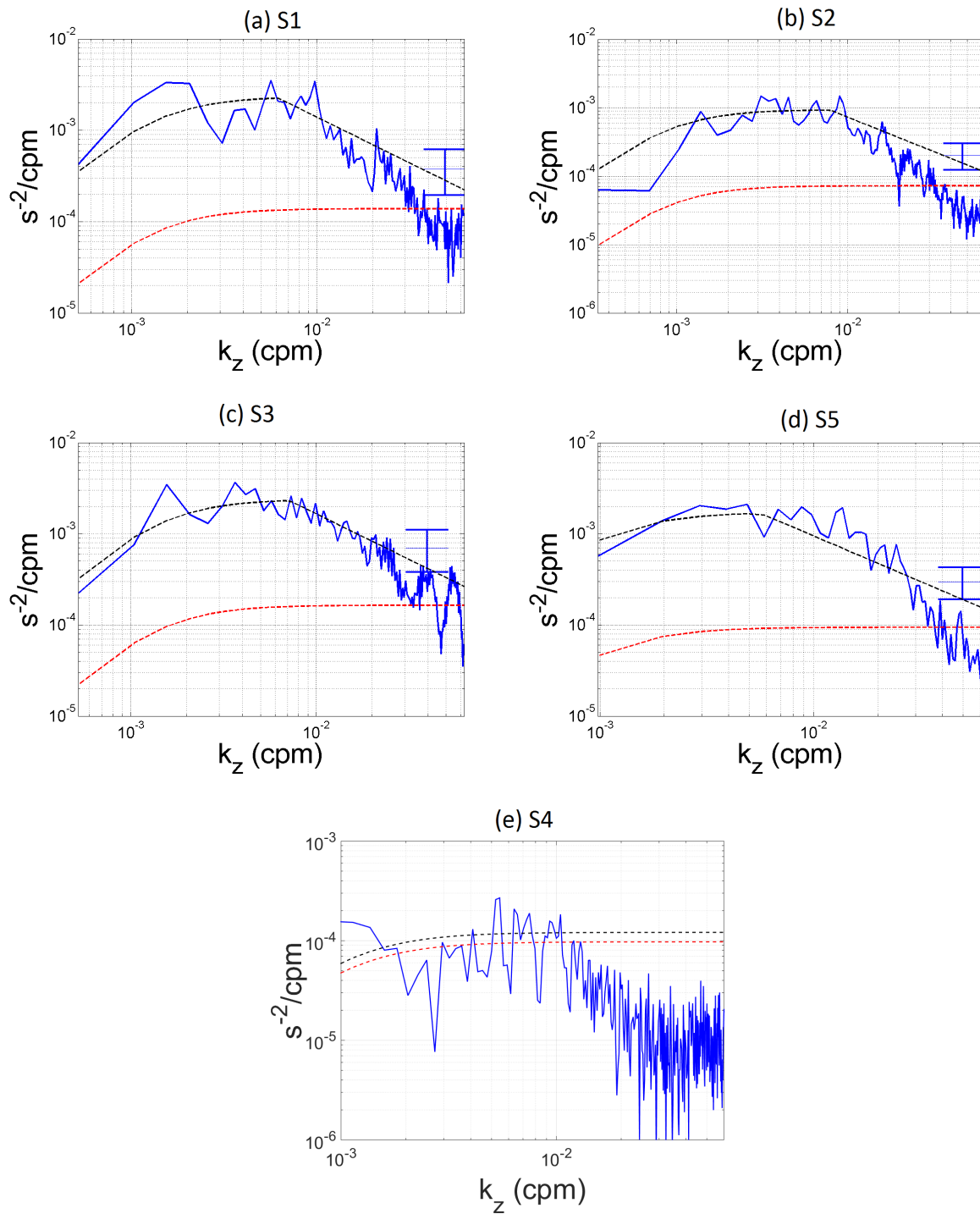


Figure 3: Observed shear spectra from LADCP (blue), canonical GM spectra (red) and GM spectra fitted to the observed shear variance (black). Ratios between observed and canonical GM shear variances computed up to $k_c = 1/100$ cpm are equal to: 17, 13, 15, 18 and 1.2 for stations S_1 , S_2 , S_3 , S_5 and S_4 . The 95% confidence interval is shown with an error bar.

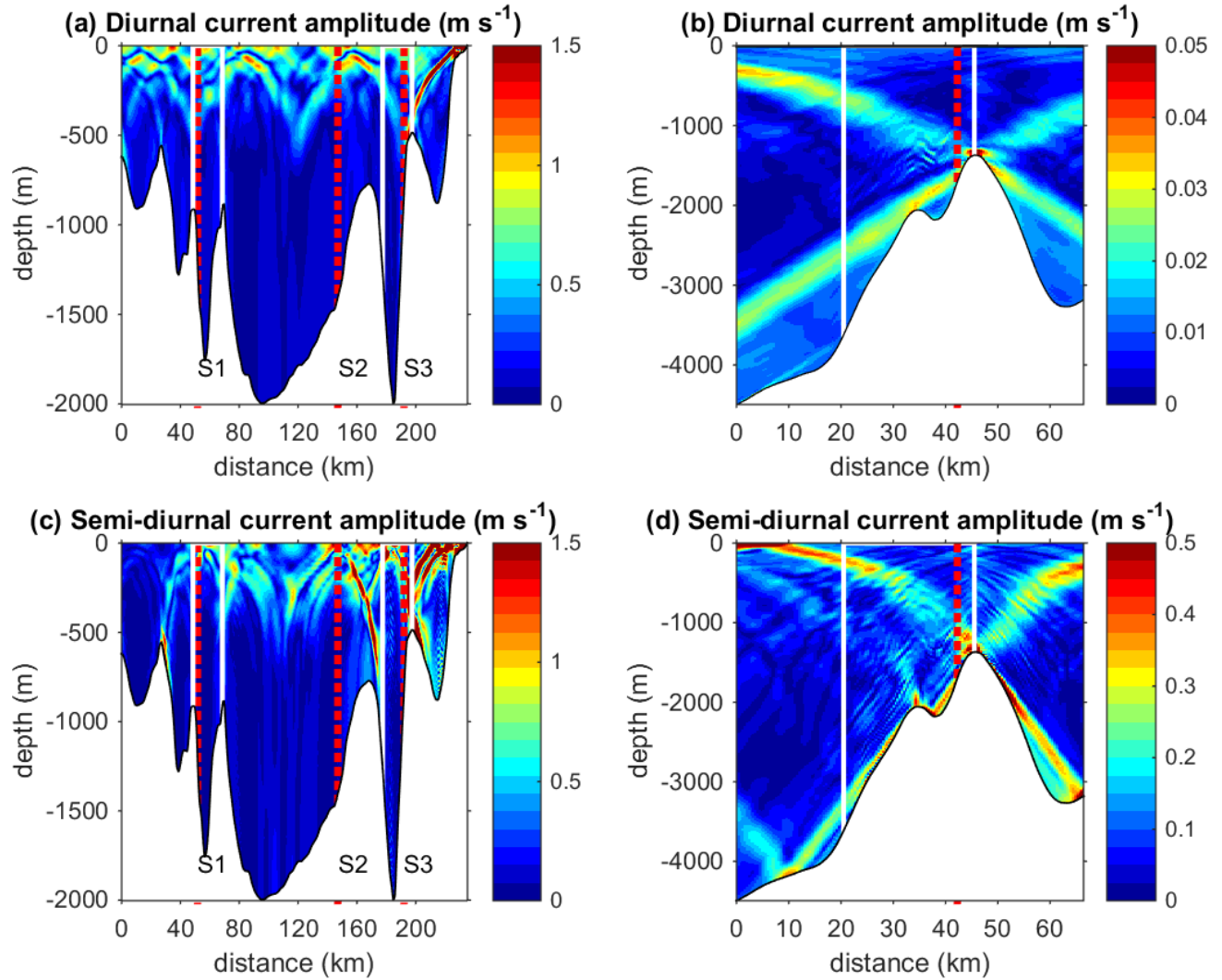


Figure 4: Vertical sections of internal tide current amplitude inferred from a 2D-linear generation model: for the Halmahera Sea (a, c) and for the Ombai Strait (b, d). Panels (c, d) show the semi-diurnal M_2 internal tide, panels (a, b) the diurnal K_1 internal tide. The vertical section passes through stations S_1 , S_2 and S_3 , which are shown as dotted red lines in (a, c) and similarly for station S_5 in (b, d). White vertical lines denote the maximum extent of regions in which some baroclinic modes propagating against barotropic flows are trapped.

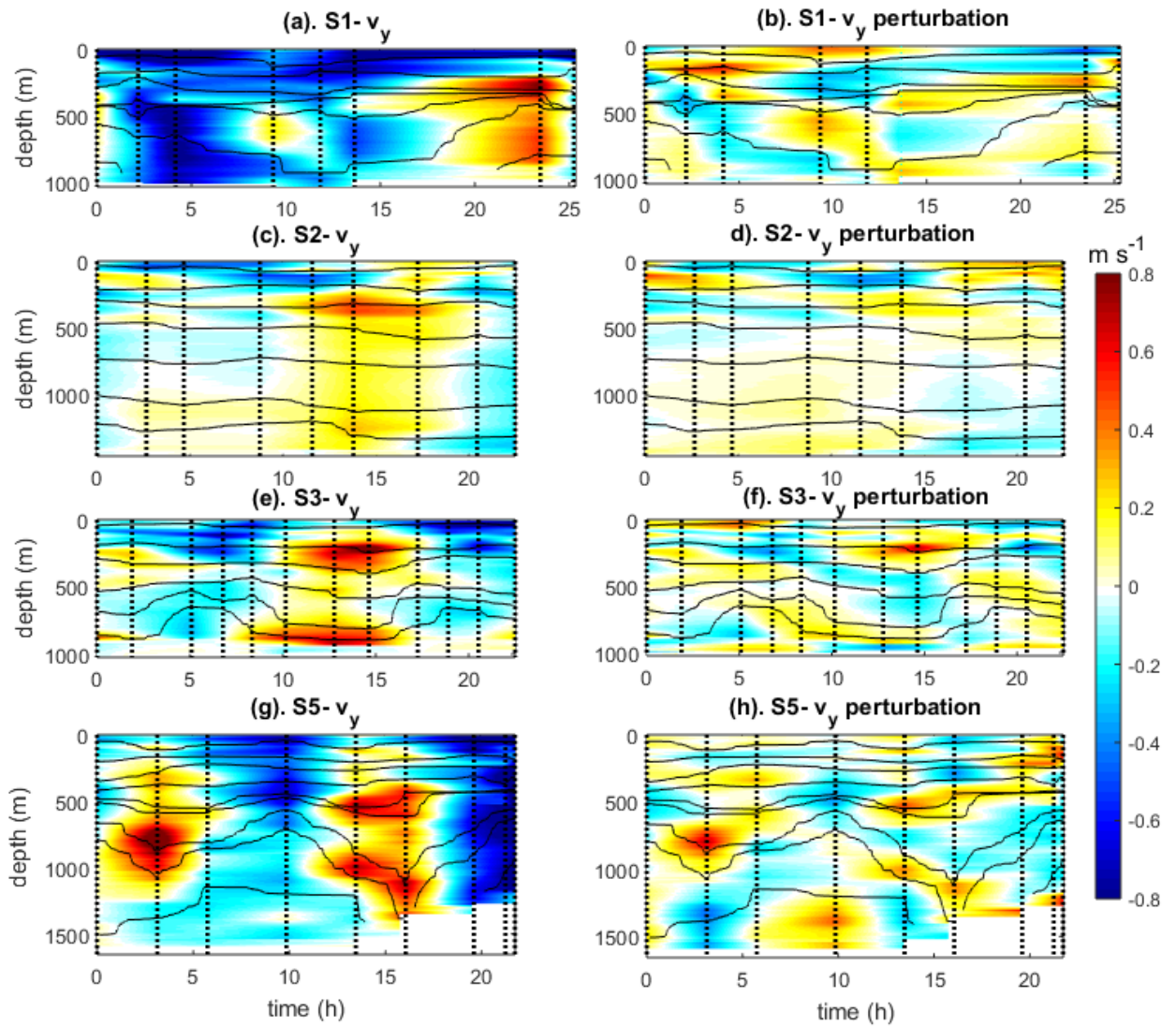


Figure 5: Total meridional currents (m s^{-1} , 1st column) and baroclinic meridional currents minus the time averaged current (m s^{-1} , 2nd column) from LADCP with isopycnals inferred from sorted density profiles superimposed with the following values: [1022;1025.5;1026.25;1026.75;1026.95;1027] in (a)-(b), [1022;1025.5;1026.5;1026.90;1026.97;1026.99] in (c)-(d), [1022;1025.5;1026.5;1026.90;1026.95;1027] in (e)-(f), [1022;1025.5;1026.25;1026.75;1026.95;1027.2;1027.4] in (g)-(h) . Each line corresponds to a station: S_1 , S_2 , S_3 and S_5 respectively. The starting time of each LADCP profile appears as a vertical gray dashed line.

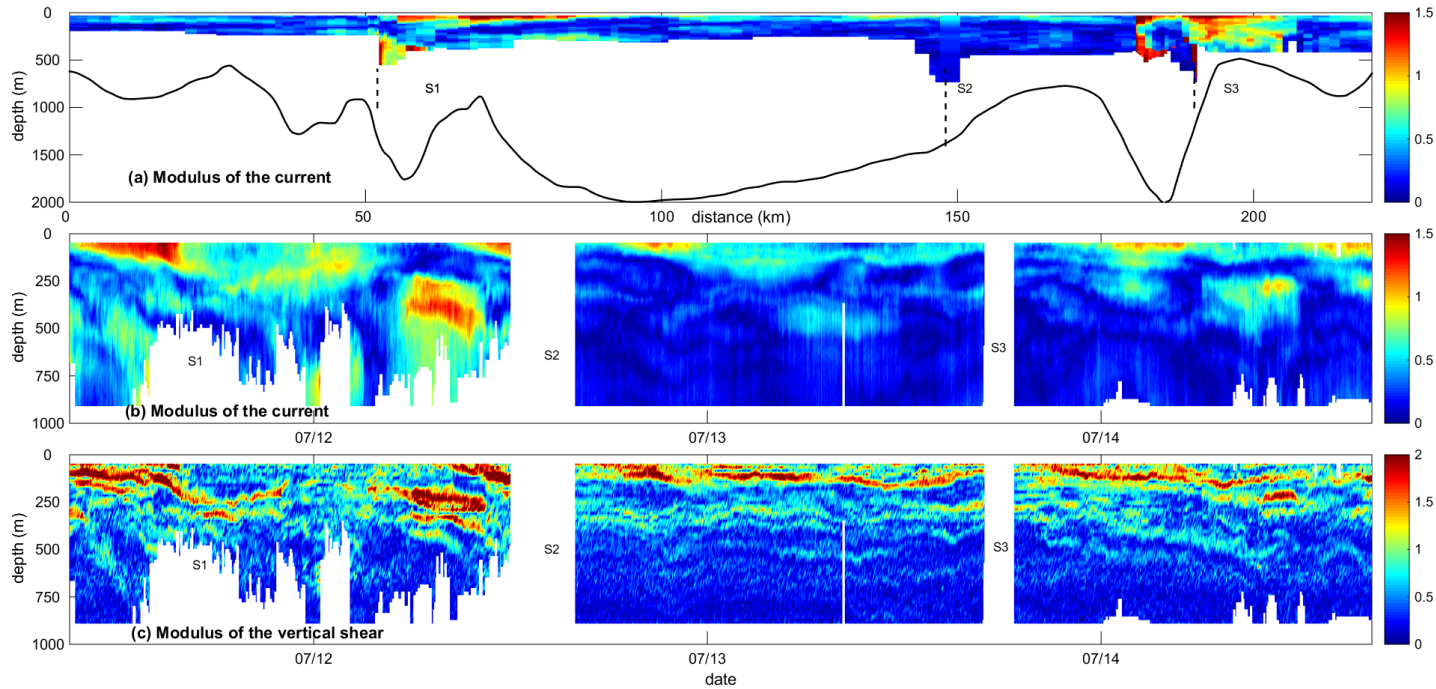


Figure 6: Vertical section of the modulus of the horizontal current magnitudes in m s^{-1} from SADC data passing through the three stations of the Halmahera Sea (a). SADC data were time averaged over two M_2 tidal cycles at the location of the three stations in (a). Vertical sections of time series at stations S_1 , S_2 and S_3 of the modulus of the horizontal current and of its vertical shear are shown in (b) and (c).

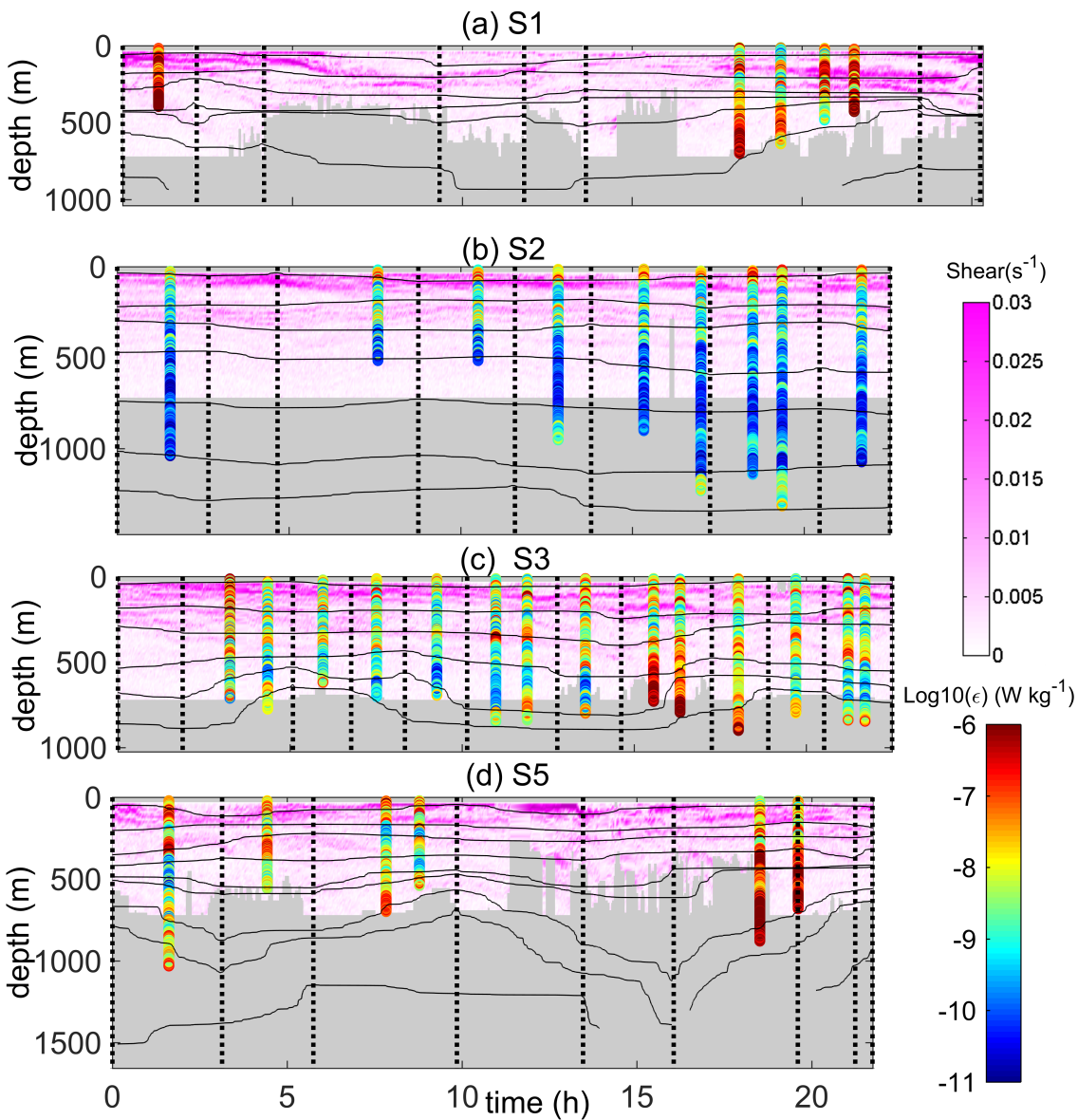


Figure 7: Dissipation rate from velocity microstructure (color log-scale, units in $W kg^{-1}$), vertical shear of horizontal velocities from ship-ADCP (magenta colorscale, from 0 to $0.03 s^{-1}$, gray when no data) and isopycnals inferred from sorted density profiles (same black contours as in Figure 5) as a function of time for the stations S_1 - S_3 in the Halmahera Sea and S_5 in the Ombai Strait. Black vertical dotted lines denote the time location of the CTD casts. Note that the maximum depth of each subplot corresponds to the maximum station depth.

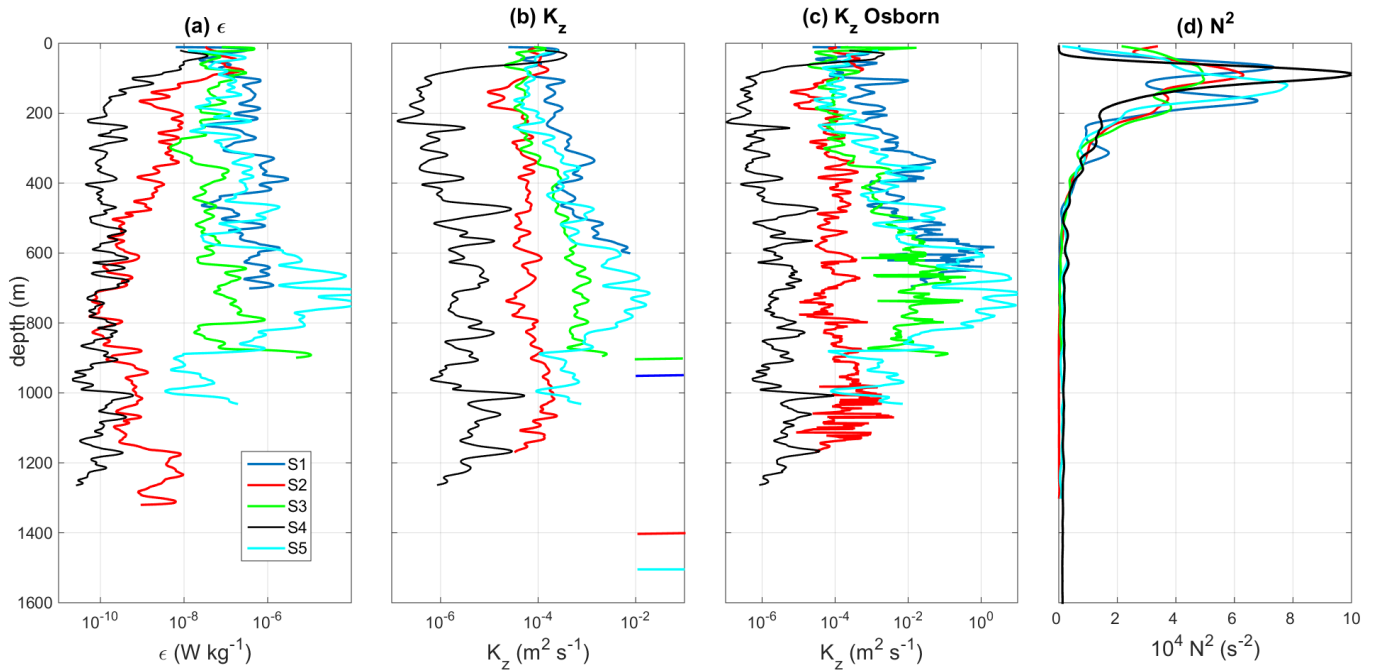


Figure 8: Time-mean profiles of energy dissipation rate ϵ , (a), vertical diffusion coefficient K_z , (b), vertical diffusion coefficient based on Osborn method $K_{z \text{ Osborn}}$, (c), and buoyancy frequency square N^2 , (d), for the 5 stations. Note that a 10-meter moving average has been applied for better visualization. Maximum values and standard deviations are listed in Tables 2 and 3. The bottom depth of the stations is indicated in (d) by an horizontal colored line except for station S_4 whose bottom depth is 4750 m.

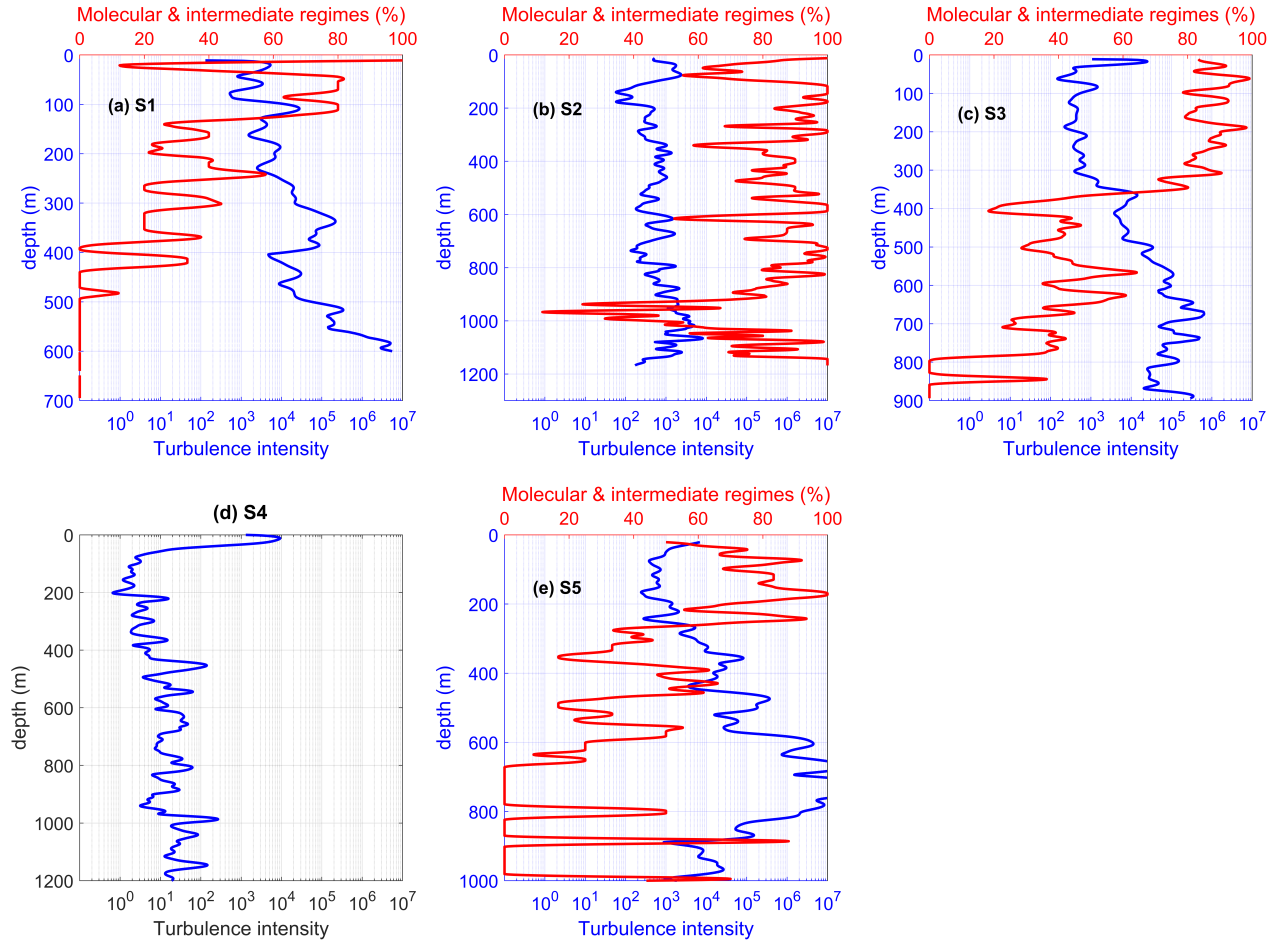


Figure 9: Time-averaged profiles of turbulence intensity (blue) for stations S_1 , S_2 , S_3 , and S_5 and percentage of occurrence of $I < 1000$ (red). The turbulence intensity profile for the single profile of station S_4 plotted is shown. All curves have been smoothed using a 10-m moving average for clarity.

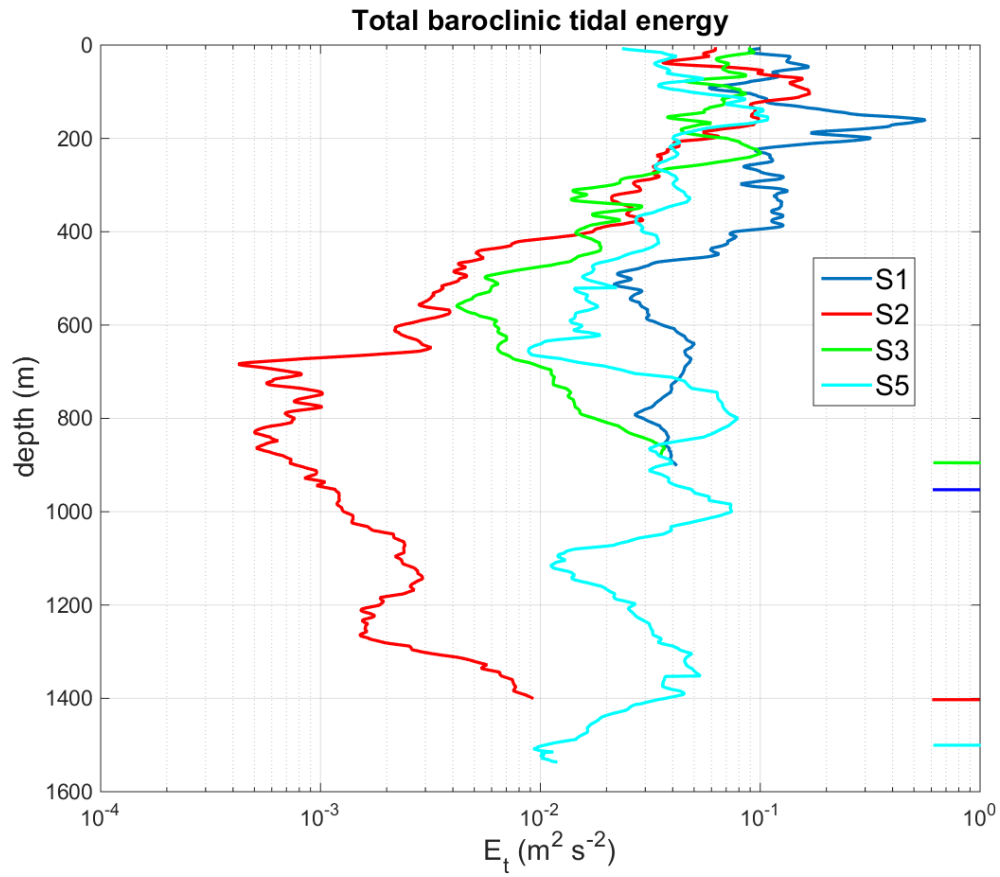


Figure 10: Mean profiles of total baroclinic tidal energy for the 4 stations (diurnal+semi-diurnal).

The bottom depth of the stations is indicated by an horizontal colored line.

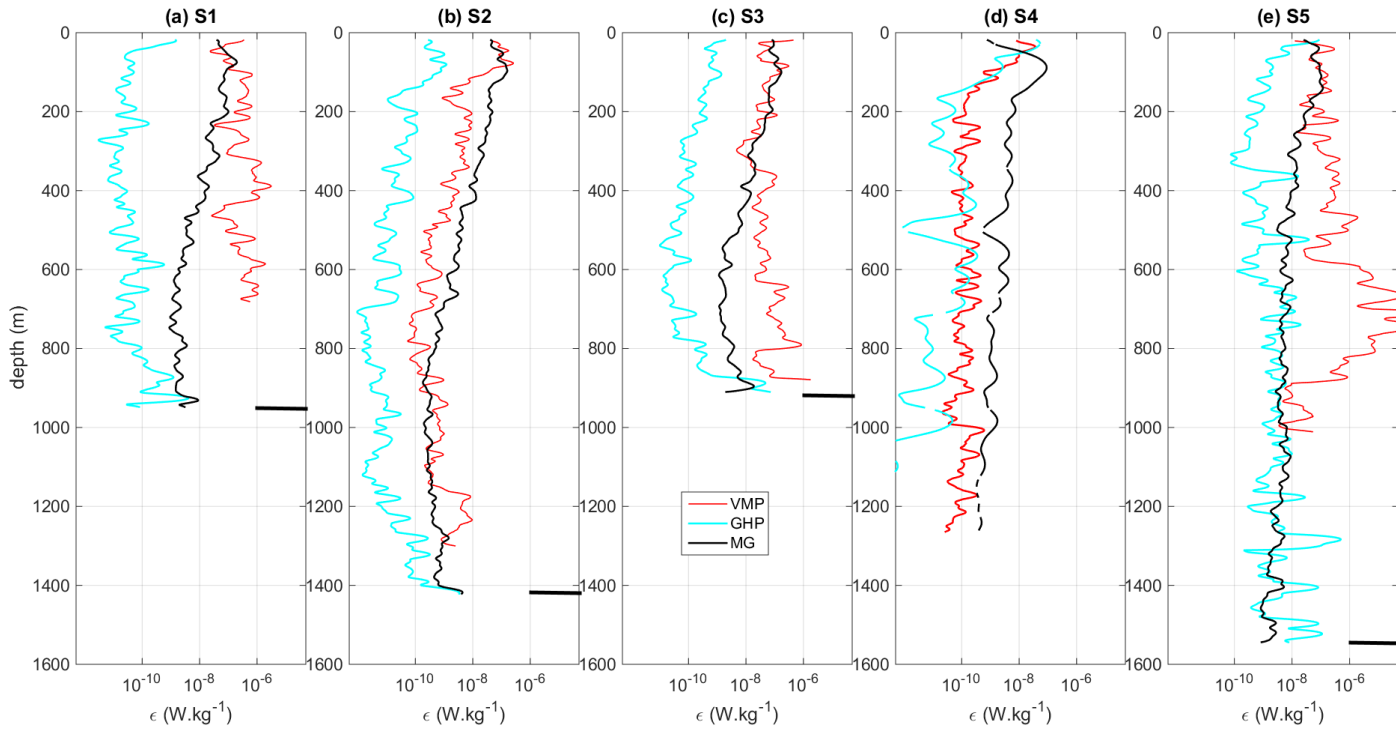


Figure 11: Mean profiles of ϵ derived from finescale parameterizations and from VMP measurements are compared at each station. The bottom depth of the stations is indicated by a black horizontal line except for station S₄.

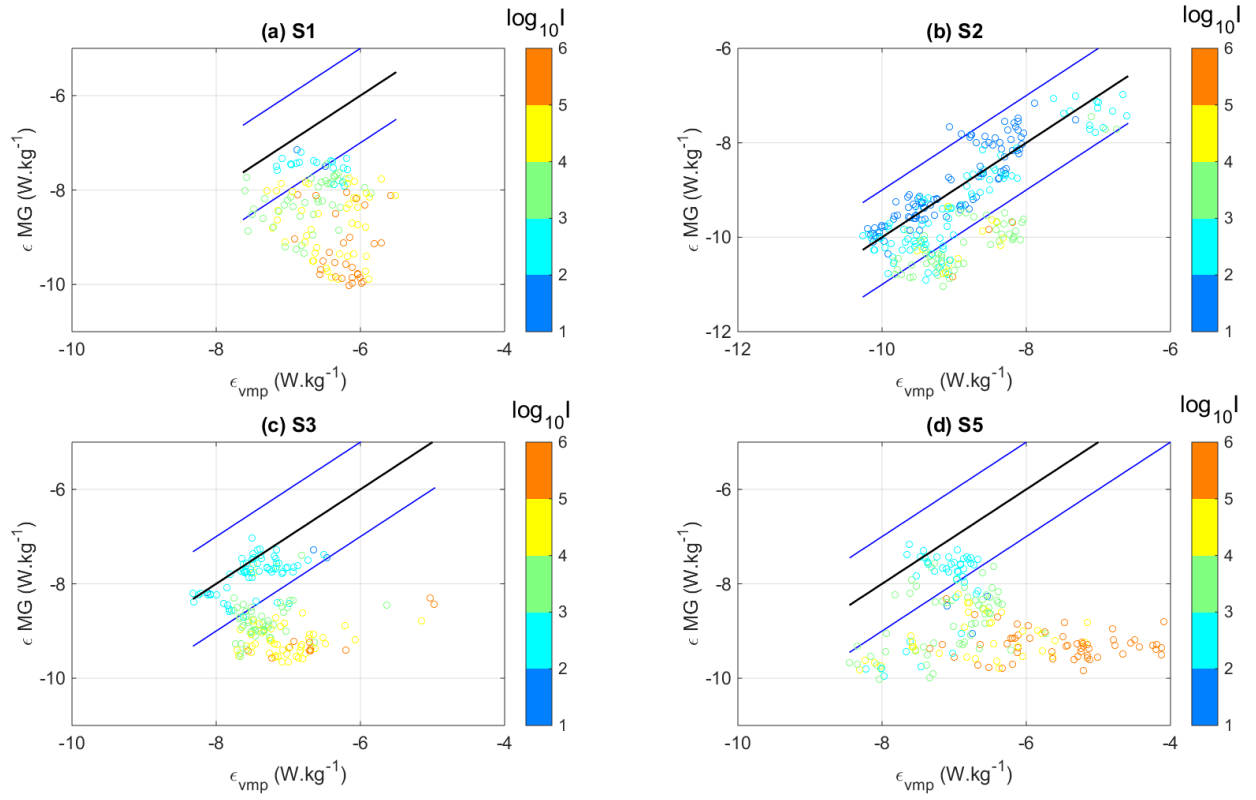


Figure 12: Mean profiles of ϵ derived from MG finescale parameterization, ϵ_{MG} , for stations S_1 , S_2 , S_3 and S_5 , as a function of ϵ_{VMP} with turbulence intensity displayed in color. Black lines (resp. blue) denote a perfect agreement (resp. a factor of 10) between blue ϵ_{MG} and ϵ_{VMP} .

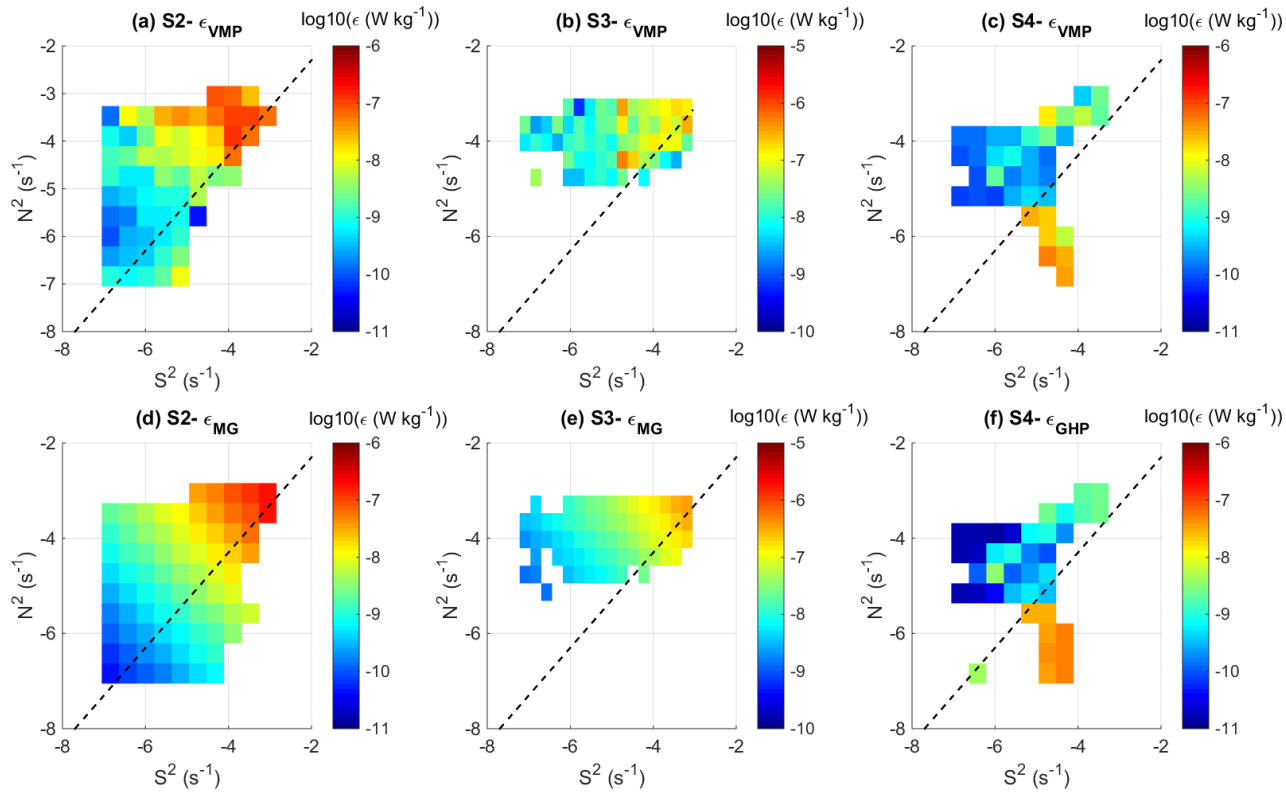


Figure 13: Bin-averaged dissipation rate (first row: ϵ_{VMP} ; second row: parameterization) as a function of shear and stratification: station S₂ (a) and (d), upper 300 m of station S₃ (b) and (e), station S₄ (c) and (f). Critical Richardson number, $Ri = 0.25$, is shown as a black dashed line. Note all CTD and LADCP profiles were included for the parameterized ϵ and not only those performed when VMP profiles were available.

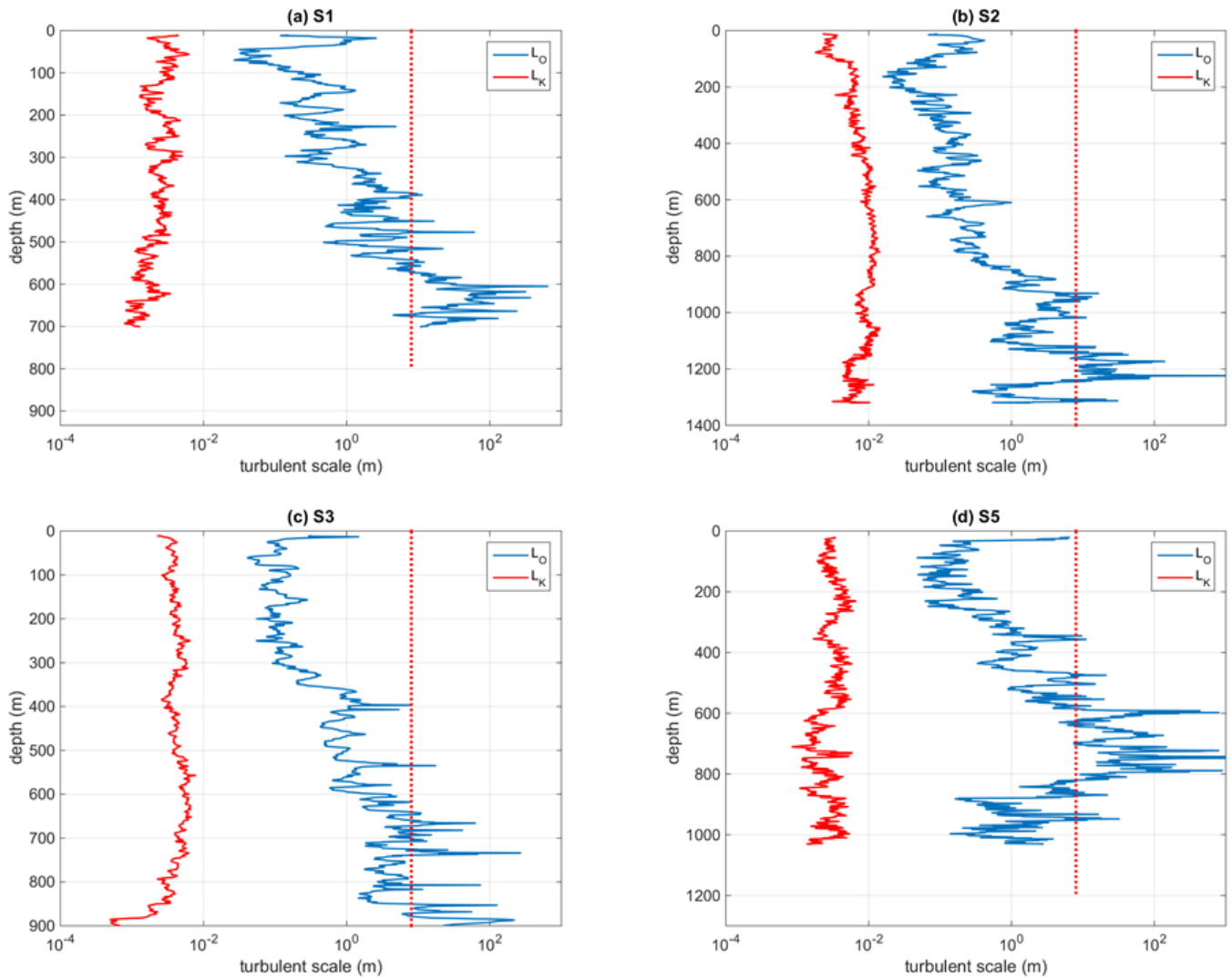


Figure 14: Mean profiles of Ozmidov and Kolmogorov scales as a function of depth for station S₁ (a), station S₂ (b), station S₃ (c) and station S₅ (d). The red dotted line denotes the vertical LADCP bin size (8 m).

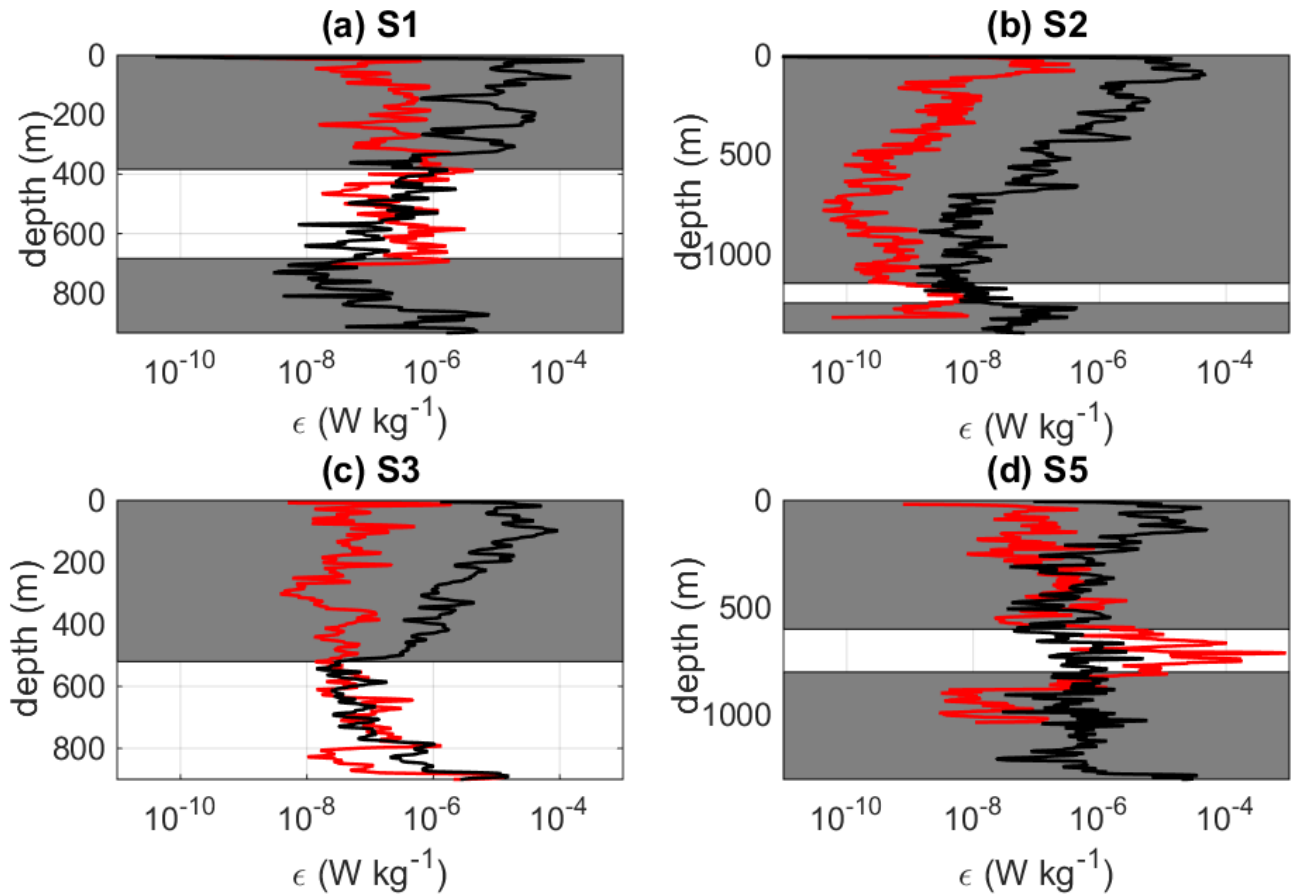


Figure 15: Mean profile of ϵ_{VMP} (red curve) and ϵ_{IR} (black curve) as a function of depth for station S_1 (a), station S_2 (b), station S_3 (c) and station S_5 (d). A 10-m moving average was applied to the mean profiles of ϵ_{VMP} and ϵ_{IR} for clarity. Gray shaded regions indicate depth intervals where ϵ_{IR} is not relevant (mean Ozmidov scale smaller than 8 m).

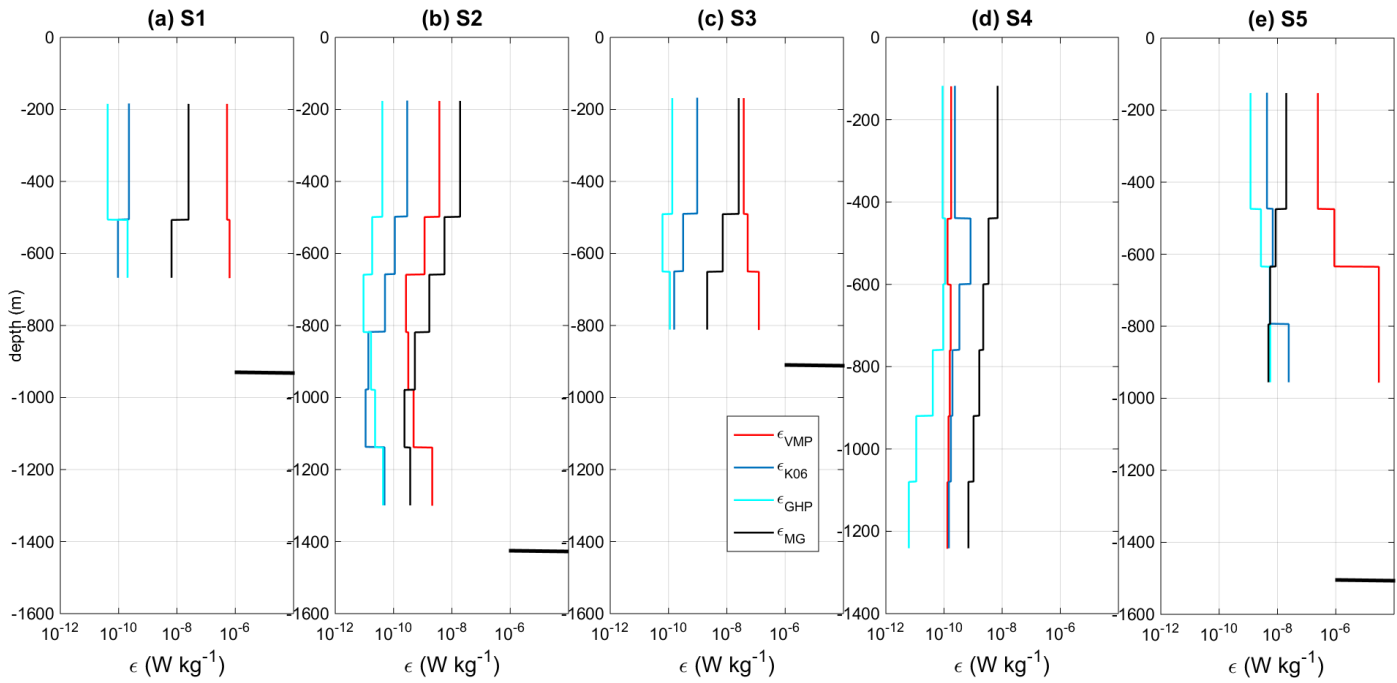


Figure 16: Mean profiles of ϵ derived from the [Kunze et al. \(2006\)](#) finescale parameterization at all stations, ϵ_{K06} is shown in blue, and $\langle \epsilon_{\text{VMP}} \rangle$ averaged over the 320 m computation intervals with an overlap of 160 m in red. $\langle \epsilon_{\text{GHP}} \rangle$ is shown as well for comparison. The bottom depth of the stations is indicated by a black horizontal line except for station S_4 .

Table 1: Position of the stations, depths and number of VMP profiles, maximum and mean of barotropic velocity modulus.

| Station | position | averaged station depth (m) | number of VMP | maximum depth of VMP | $\max(v_{btp})$ ($m s^{-1}$) | $\text{mean}(v_{btp})$ ($m s^{-1}$) |
|----------------|----------------------|-------------------------------|------------------|-------------------------|-----------------------------------|--|
| S ₁ | 129.1742E 0.0605N | 962 | 5 | 720 | 0.71 | 0.32 |
| S ₂ | 128.8830E 0.7520S | 1407 | 10 | 1340 | 0.17 | 0.09 |
| S ₃ | 129.7630E 1.1357S | 914 | 14 | 900 | 0.28 | 0.17 |
| S ₄ | 126.9980E 6.2855S | 4750 | 1 | 1270 | - | - |
| S ₅ | 125.2440E 8.2838S | 1501 | 6 | 1010 | 0.86 | 0.25 |

Table 2: Mean, standard deviation and extrema of ϵ_{VMP} ($W kg^{-1}$) and of K_z ($m^2 s^{-1}$). The average and standard deviation, σ , were first computed over time and next averaged over depth. The average of $K_{zOsborn}$ is displayed for comparison.

| Station | ϵ_{arith} | σ_{arith} | ϵ_{min} | ϵ_{max} | |
|----------------|-----------------------|----------------------|-----------------------|----------------------|----------------------|
| S ₁ | 4.9×10^{-7} | 6.4×10^{-7} | 4.3×10^{-11} | 4.2×10^{-5} | |
| S ₂ | 9.1×10^{-9} | 1.5×10^{-8} | 1.0×10^{-11} | 5.8×10^{-6} | |
| S ₃ | 2.8×10^{-7} | 2.3×10^{-7} | 1.0×10^{-11} | 6.2×10^{-5} | |
| S ₄ | 9.4×10^{-10} | 3.9×10^{-9} | 2.1×10^{-11} | 3.6×10^{-8} | |
| S ₅ | 9.8×10^{-6} | 1.5×10^{-5} | 1.1×10^{-11} | 3.5×10^{-3} | |
| Station | $(K_z)_{arith}$ | σ_{arith} | $(K_z)_{min}$ | $(K_z)_{max}$ | $(K_z)_{Osborn}$ |
| S ₁ | 9.4×10^{-4} | 7.0×10^{-4} | 2.6×10^{-5} | 2.2×10^{-2} | 4.7×10^{-2} |
| S ₂ | 7.6×10^{-5} | 7.1×10^{-5} | 6.0×10^{-6} | 4.4×10^{-4} | 1.9×10^{-4} |
| S ₃ | 3.7×10^{-4} | 4.9×10^{-4} | 1.8×10^{-5} | 3.1×10^{-3} | 1.1×10^{-2} |
| S ₄ | 1.2×10^{-5} | 5.0×10^{-5} | 1.0×10^{-7} | 4.2×10^{-4} | 3.7×10^{-5} |
| S ₅ | 1.9×10^{-3} | 2.7×10^{-3} | 2.4×10^{-5} | 2.3×10^{-2} | 4.9×10^{-1} |

Table 3: Same as Table 2 but within the thermocline. The depth range for thermocline statistics is [50 – 200]m except at station S₄ with a [50 – 120]m depth range.

| Station | ϵ_{arith} | σ_{arith} | ϵ_{min} | ϵ_{max} |
|----------------|---------------------------|-------------------------|-------------------------|-------------------------|
| S ₁ | 3.1×10^{-7} | 4.9×10^{-7} | 6.5×10^{-11} | 9.1×10^{-6} |
| S ₂ | 4.2×10^{-8} | 5.9×10^{-8} | 3.8×10^{-11} | 3.9×10^{-6} |
| S ₃ | 7.7×10^{-8} | 2.1×10^{-7} | 6.3×10^{-11} | 1.0×10^{-5} |
| S ₄ | 4.9×10^{-9} | 3.6×10^{-9} | 5.8×10^{-10} | 1.2×10^{-8} |
| S ₅ | 9.4×10^{-8} | 1.5×10^{-7} | 5.2×10^{-11} | 4.5×10^{-6} |

| Station | $(K_z)_{\text{arith}}$ | σ_{arith} | $(K_z)_{\text{min}}$ | $(K_z)_{\text{max}}$ | $(K_z)_{\text{Osborn}}$ |
|----------------|------------------------|-------------------------|----------------------|----------------------|-------------------------|
| S ₁ | 1.7×10^{-4} | 1.9×10^{-4} | 1.0×10^{-7} | 2.0×10^{-3} | 1.2×10^{-3} |
| S ₂ | 5.2×10^{-5} | 6.1×10^{-5} | 1.0×10^{-7} | 5.0×10^{-4} | 1.3×10^{-4} |
| S ₃ | 4.6×10^{-5} | 6.4×10^{-5} | 1.0×10^{-7} | 7.0×10^{-4} | 9.5×10^{-5} |
| S ₄ | 1.8×10^{-5} | 4.3×10^{-5} | 1.0×10^{-7} | 2.0×10^{-4} | 3×10^{-5} |
| S ₅ | 6.4×10^{-5} | 6.9×10^{-5} | 5.3×10^{-7} | 4.0×10^{-4} | 1.2×10^{-4} |

Table 4: Percentage of agreement within a factor of 10 (1st column), 5 (2nd column) and 2 (3rd column) of ϵ_{IR} for data such that $L_O > 8$ m.

| Station | $\epsilon_{\text{IR}}/\epsilon$ within $[1/10, 10]$ | $\epsilon_{\text{IR}}/\epsilon$ within $[1/5, 5]$ | $\epsilon_{\text{IR}}/\epsilon$ within $[1/2, 2]$ |
|----------------|---|---|---|
| S ₁ | 94 % | 86% | 78% |
| S ₂ | 73 % | 62% | 44% |
| S ₃ | 91 % | 85% | 75% |
| S ₅ | 88 % | 85% | 77% |

807 REFERENCES

- 808 Alford, M., M. C. Gregg, and M. Ilyas, 1999: Diapycnal mixing in the Banda Sea: Results
809 of the first microstructure measurements in the Indonesian Throughflow. *Geophys. Res.*
810 *Lett.*, **26 (17)**, 2741–2744.
- 811 Alford, M. H. and M. C. Gregg, 2001: Near-inertial mixing: Modulation of shear, strain
812 and microstructure at low latitude. *Journal of Geophysical Research*, **106 (C8)**, 16 947–
813 16 968.
- 814 Atmadipoera, A., A. Koch-Larrouy, G. Madec, J. Grelet, I. Jaya, I. Nurjaya, and M. Purba,
815 2017: Hydrological measurements within the Indonesian throughflow region: from
816 INDOMIX cruise 2010; (in preparation).
- 817 Atmadipoera, A., R. Molcard, G. Madec, S. Wijffels, J. Sprintall, A. Koch-Larrouy, I. Jaya,
818 and A. Supangat, 2009: Characteristics and variability of the Indonesian Throughflow
819 water at the outflow straits. *Deep Sea Research Part I: Oceanographic Research Papers*,
820 **56 (11)**, 1942–1954.
- 821 Baines, P., 1982: On internal tide generation models. *Deep Sea Research Part A. Oceano-*
822 *graphic Research Papers*, **29 (3)**, 307–338.
- 823 Beaird, N., I. Fer, P. Rhines, and C. Eriksen, 2012: Dissipation of turbulent kinetic energy
824 inferred from seagliders. *Journal of Physical Oceanography*, **42**, 2268–2282.

- 825 Bluteau, C., N. Jones, and G. Ivey, 2013: Turbulent mixing efficiency at an energetic ocean
826 site. *Journal of Geophysical Research: Oceans*, **118** (9), 4662–4672.
- 827 Bouffard, D. and L. Boegman, 2013: A diapycnal diffusivity model for stratified environ-
828 mental flows. *Dynamics of Atmospheres and Oceans*, **61**, 14–34.
- 829 Bouruet-Aubertot, P., J. Sommeria, and C. Staquet, 1995: Breaking of standing internal
830 gravity waves through two-dimensional instabilities. *Journal of Fluid Mechanics*, **285**,
831 265–301.
- 832 Buijsman, M. C., S. Legg, and J. Klymak, 2012: Double-ridge internal tide interference
833 and its effect on dissipation in luzon strait. *Journal of Physical Oceanography*, **42** (8),
834 1337–1356.
- 835 Canuto, C., A. Quarteroni, M. Hussaini, and T. Zang, 1988: Spectral method in fluid
836 mechanics. Springer-Verlag, New York.
- 837 Cuypers, Y., P. Bouruet-Aubertot, C. Marec, and J.-L. Fuda, 2012: Characterization of
838 turbulence from a fine-scale parameterization and microstructure measurements in
839 the Mediterranean Sea during the BOUM experiment. *Biogeosciences*, **9** (8), 3131–3149.
- 840 De Lavergne, C., G. Madec, J. Le Sommer, A. G. Nurser, and A. C. Naveira Garabato,
841 2016a: The impact of a variable mixing efficiency on the abyssal overturning. *Journal*
842 *of Physical Oceanography*, **46** (2), 663–681.
- 843 De Lavergne, C., G. Madec, J. Le Sommer, A. G. Nurser, and A. C. Naveira Garabato,
844 2016b: On the consumption of antarctic bottom water in the abyssal ocean. *Journal of*
845 *Physical Oceanography*, **46** (2), 635–661.

- 846 Egbert, G. and R. Ray, 2000: Significant dissipation of tidal energy in the deep ocean
847 inferred from satellite altimeter data. *Nature*, **405 (6788)**, 775–778.
- 848 Egbert, G. D. and S. Y. Erofeeva, 2002: Efficient inverse modeling of barotropic ocean
849 tides. *Journal of Atmospheric and Oceanic Technology*, **19 (2)**, 183–204.
- 850 Egbert, G. D. and R. D. Ray, 2003: Semi-diurnal and diurnal tidal dissipation from
851 TOPEX/POSEIDON altimetry. *Geophysical Research Letters*, **30 (17)**, 1907.
- 852 Ferron, B., F. Kokoszka, H. Mercier, and P. Lherminier, 2014: Dissipation rate esti-
853 mates from microstructure and finescale internal wave observations along the A25
854 Greenland-Portugal OVIDE line. *Journal of Atmospheric and Oceanic Technology*, **31**, 2530–
855 2543.
- 856 Ffield, A. and A. L. Gordon, 1992: Vertical mixing in the Indonesian thermocline. *Journal*
857 *of Physical Oceanography*, **22 (2)**, 184–195.
- 858 Ffield, A. and A. L. Gordon, 1996: Tidal mixing signatures in the Indonesian Seas. *Journal*
859 *of Physical Oceanography*, **26 (9)**, 1924–1937.
- 860 Ffield, A. and R. Robertson, 2005: Indonesian Seas finestructure variability. *Oceanography*,
861 **18 (4)**, 108–111.
- 862 Ffield, A. and R. Robertson, 2008: Temperature finestructure in the Indonesian Seas.
863 *Journal of Geophysical Research*, **113 (C9)**, C09 009.
- 864 Garrett, C. and W. Munk, 1975: Space-time scales of internal waves: A progress report.
865 *Journal of Geophysical Research*, **80 (3)**, 291–297.

- 866 Gayen, B. and S. Sarkar, 2011: Boundary mixing by density overturns in an internal tidal
867 beam. *Geophysical Research Letters*, **38** (14).
- 868 Gerkema, T., F.-P. A. Lam, and L. R. Maas, 2004: Internal tides in the Bay of Biscay: con-
869 version rates and seasonal effects. *Deep Sea Research Part II: Topical Studies in Oceanogra-
870 phy*, **51** (25), 2995–3008.
- 871 Gordon, A., et al., 2010: The Indonesian Throughflow during 2004–2006 as observed by
872 the INSTANT program. *Dynamics of Atmospheres and Oceans*, **50** (2), 115–128.
- 873 Gordon, A. L., 1986: Interocean exchange of thermocline water. *Journal of Geophysical
874 Research: Oceans (1978–2012)*, **91** (C4), 5037–5046.
- 875 Gordon, A. L., 2005: The Indonesian Seas. *Oceanography*, **18** (4), 14–27.
- 876 Gordon, A. L. and R. A. Fine, 1996: Pathways of water between the Pacific and Indian
877 Oceans in the Indonesian Seas. *Nature*, **379** (6561), 146–149.
- 878 Gregg, M., 1989: Scaling turbulent dissipation in the thermocline. *Journal of Geophysical
879 Research*, **94** (C7), 9686–9698.
- 880 Gregg, M., M. Alford, H. Kontoyiannis, V. Zervakis, and D. Winkel, 2012: Mixing over
881 the steep side of the cycladic plateau in the aegean sea. *Journal of Marine Systems*, **89** (1),
882 30–47.
- 883 Gregg, M. C., T. B. Sanford, and D. P. Winkel, 2003: Reduced mixing from the breaking
884 of internal waves in equatorial waters. *Nature*, **422** (6931), 513–515.

- 885 Henyey, F. S., J. Wright, and S. M. Flatté, 1986: Energy and action flow through the
886 internal wave field: An eikonal approach. *Journal of Geophysical Research: Oceans* (1978–
887 2012), **91** (C7), 8487–8495.
- 888 Huussen, T., A. Naveira-Garabato, H. Bryden, and E. McDonagh, 2012: Is the deep
889 indian ocean moc sustained by breaking internal waves? *Journal of Geophysical Research:*
890 *Oceans*, **117** (C8).
- 891 Klymak, J. M., S. Legg, and R. Pinkel, 2010: A simple parameterization of turbulent
892 mixing near supercritical topography. *Journal of Physical Oceanography*, **40** (9), 2059–
893 2074.
- 894 Koch-Larrouy, A., A. Atmadipoera, P. Van Beek, G. Madec, J. Aucas, F. Lyard, J. Grelet,
895 and M. Souhaut, 2015: Estimates of tidal mixing in the indonesian archipelago from
896 multidisciplinary indomix in-situ data. *Deep Sea Research Part I: Oceanographic Research*
897 *Papers*, **106**, 136–153.
- 898 Koch-Larrouy, A., G. Madec, D. Iudicone, A. Atmadipoera, and R. Molcard, 2008:
899 Physical processes contributing to the water mass transformation of the Indonesian
900 Throughflow. *Ocean Dynamics*, **58** (3-4), 275–288.
- 901 Kunze, E., E. Firing, J. M. Hummon, T. K. Chereskin, and A. M. Thurnherr, 2006: Global
902 abyssal mixing inferred from lowered ADCP shear and CTD strain profiles. *Journal of*
903 *Physical Oceanography*, **36** (8), 1553–1576.

- 904 Legg, S. and K. M. Huijts, 2006: Preliminary simulations of internal waves and mixing
905 generated by finite amplitude tidal flow over isolated topography. *Deep Sea Research*
906 *Part II: Topical Studies in Oceanography*, **53 (1)**, 140–156.
- 907 Lelong, M. and T. Dunkerton, 1998a: Inertia-gravity wave breaking in three dimensions.
908 part i: convectively stable waves. *Journal of Atmospheric Sciences*, **55 (15)**, 2473–2488.
- 909 Lelong, M. and T. Dunkerton, 1998b: Inertia-gravity wave breaking in three dimensions.
910 part ii: convectively unstable waves. *Journal of Atmospheric Sciences*, **55 (15)**, 2489–2501.
- 911 Lelong, M.-P. and E. Kunze, 2013: Can barotropic tide–eddy interactions excite internal
912 waves? *Journal of Fluid Mechanics*, **721**, 1–27.
- 913 Llewellyn Smith, S. G. and W. Young, 2003: Tidal conversion at a very steep ridge. *Journal*
914 *of Fluid Mechanics*, **495**, 175–191.
- 915 Lyard, F. and C. Le Provost, 2002: Energy budget of the tidal hydrodynamic model
916 fes99. Appears in C. Le Provosts' talk: "Ocean tides after a decade of high precision satellite
917 altimetry", *SWT Jason*, **1**.
- 918 MacKinnon, J. and M. Gregg, 2003: Mixing on the late-summer New England Shelf-
919 solibores, shear, and stratification. *Journal of Physical Oceanography*, **33 (7)**, 1476–1492.
- 920 MacKinnon, J. and M. Gregg, 2005: Spring mixing: Turbulence and internal waves dur-
921 ing restratification on the New England Shelf. *Journal of Physical Oceanography*, **33 (12)**,
922 2425–2443.

- 923 Manders, A., L. Maas, and T. Gerkema, 2004: Observations of internal tides in the
924 mozambique channel. *Journal of Geophysical Research: Oceans*, **109** (C12).
- 925 Mathur, M., G. S. Carter, and T. Peacock, 2014: Topographic scattering of the low-mode
926 internal tide in the deep ocean. *Journal of Geophysical Research: Oceans*, **119** (4), 2165–
927 2182.
- 928 McComas, C. H. and P. Müller, 1981: The dynamic balance of internal waves. *Journal of*
929 *Physical Oceanography*, **11** (7), 970–986.
- 930 Moum, J. N., 1996: Energy-containing scales of turbulence in the ocean thermocline.
931 *Journal of Geophysical Research*, **101** (C6), 14,095–14,109.
- 932 Nagai, T. and T. Hibiya, 2015: Internal tides and associated vertical mixing in the indone-
933 sian archipelago. *Journal of Geophysical Research: Oceans*, 1977–2010.
- 934 Nagai, T., T. Hibiya, and P. Bouruet-Aubertot, 2017: Nonhydrostatic simulations of tide-
935 induced mixing in the halmahera sea: A possible role in the transformation of the
936 indonesian throughflow waters. *Journal of Geophysical Research: Oceans*.
- 937 Nasmyth, P. W., 1970: Oceanic turbulence.
- 938 Naveira Garabato, A. C., K. I. Oliver, A. J. Watson, and M.-J. Messias, 2004: Turbulent
939 diapycnal mixing in the nordic seas. *Journal of Geophysical Research: Oceans*, **109** (C12).
- 940 Osborn, T., 1980: Estimates of the local rate of vertical diffusion from dissipation mea-
941 surements. *Journal of Physical Oceanography*, **10** (1), 83–89.

- 942 Pasquet, S., P. Bouruet-Aubertot, G. Reverdin, A. Turnherr, and L. St Laurent, 2016:
943 Validation of fine-scale parameterization of energy dissipation in a region of strong
944 internal tides and sheared flow, the lucky-strike segment of the mid-atlantic ridge.
945 *Deep-Sea Research*, **112**, 79–93.
- 946 Peters, H., M. C. Gregg, and T. B. Sanford, 1995: Detail and scaling of turbulent overturns
947 in the pacific equatorial undercurrent. *Journal of Geophysical Research: Oceans*, **100 (C9)**,
948 18 349–18 368.
- 949 Polzin, K., E. Kunze, J. Hummon, and E. Firing, 2002: The finescale response of lowered
950 ADCP velocity profiles. *Journal of Atmospheric and Oceanic Technology*, **19 (2)**, 205–224.
- 951 Polzin, K. L., A. C. Naveira Garabato, T. N. Huussen, B. M. Sloyan, and S. Waterman,
952 2014: Finescale parameterizations of turbulent dissipation. *Journal of Geophysical Re-*
953 *search: Oceans*, **119 (2)**, 1383–1419.
- 954 Polzin, K. L., J. M. Toole, and R. W. Schmitt, 1995: Finescale parameterizations of turbu-
955 lent dissipation. *Journal of Physical Oceanography*, **25 (3)**, 306–328.
- 956 Rainville, L., T. S. Johnston, G. S. Carter, M. A. Merrifield, R. Pinkel, P. F. Worcester,
957 and B. D. Dushaw, 2010: Interference pattern and propagation of the m 2 internal tide
958 south of the hawaiian ridge. *Journal of Physical Oceanography*, **40 (2)**, 311–325.
- 959 Robertson, R., 2010: Tidal currents and mixing at the INSTANT mooring locations. *Dy-*
960 *namics of Atmospheres and Oceans*, **50**, 331–373.
- 961 Robertson, R. and A. Ffield, 2008: Baroclinic tides in the Indonesian Seas: Tidal fields
962 and comparisons to observations. *Journal of Geophysical Research*, **113 (C7)**.

- 963 Schiller, A., S. Wijffels, J. Sprintall, R. Molcard, and P. R. Oke, 2010: Pathways of in-
964 traseasonal variability in the Indonesian throughflow region. *Dynamics of atmospheres*
965 *and oceans*, **50 (2)**, 174–200.
- 966 Shih, L. H., J. R. Koseff, G. N. Ivey, and J. H. Ferziger, 2005: Parameterization of turbulent
967 fluxes and scales using homogeneous sheared stably stratified turbulence simulations.
968 *Journal of Fluid Mechanics*, **525**, 193–214.
- 969 Simmons, H. L., R. W. Hallberg, and B. K. Arbic, 2004: Internal wave generation in a
970 global baroclinic tide model. *Deep Sea Research Part II: Topical Studies in Oceanography*,
971 **51 (25)**, 3043–3068.
- 972 Sprintall, J., et al., 2004: Instant: A new international array to measure the Indonesian
973 Throughflow. *Eos, Transactions American Geophysical Union*, **85 (39)**, 369–376.
- 974 St Laurent, L. C. and A. M. Thurnherr, 2007: Intense mixing of lower thermocline water
975 on the crest of the mid-atlantic ridge. *Nature*, **448 (7154)**, 680–683.
- 976 Taylor, G. I., 1935: Statistical theory of turbulence. *Proceedings of the Royal Society of London*
977 *A: Mathematical, Physical and Engineering Sciences*, The Royal Society, Vol. 151, 421–444.
- 978 Tennekes, H. and J. L. Lumley, 1972: *A first course in Turbulence*. MIT press.
- 979 van Haren, H., A. Cimadoribus, and L. Gostiaux, 2015: Where large deep-ocean waves
980 break. *Geophysical Research Letters*, **42 (7)**, 2351–2357.

- 981 Visbeck, M., 2002: Deep velocity profiling using lowered acoustic doppler current profil-
982 ers: Bottom track and inverse solutions*. *Journal of Atmospheric and Oceanic Technology*,
983 **19 (5)**, 794–807.
- 984 Walter, M., C. Mertens, and M. Rhein, 2005: Mixing estimates from a large-scale hydro-
985 graphic survey in the north atlantic. *Geophysical research letters*, **32 (13)**.
- 986 Waterman, S., A. C. Naveira Garabato, and K. L. Polzin, 2013: Internal waves and tur-
987 bulence in the antarctic circumpolar current. *Journal of Physical Oceanography*, **43 (2)**,
988 259–282.
- 989 Wijesekera, H., L. Padman, T. Dillon, M. Levine, C. Paulson, and R. Pinkel, 1993: The
990 application of internal-wave dissipation models to a region of strong mixing. *Journal*
991 *of Physical Oceanography*, **23**, 269–286.
- 992 Xie, X., Y. Cuyppers, P. Bouruet-Aubertot, B. Ferron, A. Pichon, A. Lourenço, and
993 N. Cortes, 2013: Large-amplitude internal tides, solitary waves, and turbulence in
994 the central Bay of Biscay. *Geophysical Research Letters*, **40**, 2748–2754.